J. Fluid Mech. (2009), *vol.* 630, *pp.* 331–365. © 2009 Cambridge University Press
doi:10.1017/S0022112009006648 Printed in the United Kingdom

Effects of wall compliance on the linear stability of Taylor–Couette flow

ANAÏS GUAUS[1]†, CHRISTOPHE AIRIAU[1], ALESSANDRO BOTTARO[2] AND AZEDDINE KOURTA[1]‡

[1]Université de Toulouse, Institut de Mécanique des Fluides, UMR 5502 CNRS/INP-UPS, Allée du Professeur Camille Soula, 31400 Toulouse, France

[2]DICAT, Università di Genova, Via Montallegro 1, 16145 Genova, Italy

(Received 2 August 2008 and in revised form 16 February 2009)

The stability of the laminar flow in the narrow gap between infinitely long concentric cylinders, the inner of which rotates, is examined for the case of compliant bounding walls, modelled as thin cylindrical shells supported by rigid frames through arrays of springs and dampers. Sufficiently soft walls have a destabilizing influence on the axisymmetric Taylor vortices produced by the centrifugal force, although the effect is limited to modes with large axial wavelengths. Due to the walls flexibility, hydroelastic modes are generated. Complex modal exchanges are observed, as function of the wall properties and the Reynolds number. For axisymmetric modes an asymptotic analysis is conducted in the limit of small axial wavenumber, to show the correspondence between such exchanges and singularities in the analytical solutions. While the axisymmetric modes dominate the spectrum when the walls are rigid or very mildly compliant, a critical non-zero azimuthal wavenumber exists for which the hydroelastic modes become more unstable. Shorter azimuthal waves are favoured by increasing spring stiffness.

1. Introduction

Studies on the effect of compliant walls on flow stability were inspired by Kramer's observation of swimming dolphins in the late 1950s (Kramer 1957, 1960*a*, *b*, 1965). Kramer assumed that their high propulsive efficiency should be ascribed to the compliance of their skin. He then carried out experiments in water by dragging a torpedo covered with a compliant device conceived to mimic the dolphin's skin and achieved drag reduction of more than 50 % compared to the rigid case. A few years later, the first theoretical work of Benjamin (1960, 1963) and Landahl (1962) focused on the linear stability of the boundary layer on a compliant flat plate modelled as a thin elastic membrane. For this configuration, simpler than Kramer's experimental one, the Tollmien–Schlichting (TS) waves, responsible for the mechanism of laminar-to-turbulent transition, are stabilized for some compliant parameters. In return, as compliant surfaces are wave-bearing media, new modes of instability can occur in the flow, in addition to those of the rigid case. These wall-induced/hydroelastic modes can influence the transition to turbulence and hinder the benefit of stabilizing TS waves.

† Email address for correspondence: anais.guaus@alumni.enseeiht.fr

‡ Present address: ESA, PRISME – Polytech'Orléans, 8 rue Léonard de Vinci, 45072 Orléans Cedex 2, France.

The most important of these surface modes are travelling-wave flutter (TWF) and static divergence (SD), which are the incompressible analogue of classical aeroelastic phenomena. They have been since extensively described in publications concerning the flat-plate boundary layer or the plane channel case (see Carpenter, Davies & Lucey 2000; Gad-El-Hak 2002, for instance) and will be only shortly described in this section. TWF has been usually identified with a high-frequency streamwise-travelling wave, when a critical flow speed, which increases with the wall stiffness, is exceeded (see Carpenter & Garrad 1985; Yeo 1988; Carpenter & Morris 1990; Davies & Carpenter 1997*a*,*b*; Lucey, Cafolla & Carpenter 1998). SD occurs in the form of very slowly travelling or stationary waves of long wavelength and, as such, can have an effect similar to that of surface roughness (Gad-el-Hak, Blackwelder & Riley 1984; Duncan, Waxman & Tulin 1985; Carpenter & Garrad 1986; Gad-el-Hak 1986; Lucey & Carpenter 1992; Yeo, Khoo & Zhao 1996; Lucey, Cafolla & Carpenter 1997*a*; Lucey *et al.* 1997*b*, 1998). The outcome of the analytical studies cited above is that, if the properties of the compliant walls are properly chosen, it is possible to stabilize the TS waves without generating new instabilities.

These successful works were the starting point for renewed interest in compliant walls in the scientific community: compliant coatings could provide a simple passive control device for many engineering applications, possibly helpful for laminar-to-turbulent transition delay, skin-friction drag reduction and flow-induced noise reduction. However, for many years, all the experiments aiming at reproducing Kramer's results were unsuccessful (Bushnell, Hefner & Ash 1977) undermining his conclusions, until Carpenter & Garrad (1985, 1986) rehabilitated his work. These latter authors proposed for the first time a theoretical wall model able to reproduce the complexity of Kramer's experimental compliant device. This model consists of a thin plate supported by a rigid foundation through springs and dampers. It was then shown that Kramer's compliant wall is theoretically able to delay transition. These results were confirmed notably by Yeo (1988) and Sen & Arora (1988) (see also Riley, Gad-El-Hak & Metcalfe 1988; Carpenter 1990). Finally, the stabilization of TS waves by compliance was proven experimentally by Gaster (1987). The understanding of the behaviour of TS waves was later deepened by considering the influence of non-parallel effects in the boundary layer (Yeo, Khoo & Chong 1994), secondary instability (Joslin & Morris 1992) and more generally nonlinearities (Ehrenstein & Rossi 1996; Lucey *et al.* 1997*a*; Wiplier & Ehrenstein 2000).

The studies cited above focused on the case of plane walls. Other kinds of configurations have been – less extensively – considered, where the transition scenario is not necessarily dominated by TS instability. Cooper & Carpenter (1997*a*,*b*), theoretically, and Colley *et al.* (1999, 2006), experimentally, considered the boundary layer transition over a compliant rotating disk, showing that the cross-flow instability, the culprit of transition, is stabilized by wall compliance. However, the second – viscous – mode has a more complex behaviour: it is destabilized when the disc is only slightly compliant, it is stabilized and finally disappears when the compliance increases (see also Carpenter & Thomas 2007). Attention has also shifted to curved-wall configurations where the flow is submitted to a centrifugal instability mechanism. Yurchenko & Babenko (1987) observed that a porous rubber coating could delay the amplification of Görtler longitudinal vortices developing over the concave wall of a water channel. A very mild stabilizing effect was found when the large Görtler number and spanwise wavenumber limits were taken (Denier & Hall 1991), but the theory did not address the behaviour of hydroelastic modes. Guaus & Bottaro (2007) have considered the instabilities of the flow in a curved compliant channel by adapting

the plane spring-based model of Carpenter & Garrad (1985) for curved walls via thin shell theory. In addition to instabilities similar to those observed in a plane channel (Davies & Carpenter 1997*a*), the study has shown that the streamwise vortices produced in the channel by the centrifugal force are destabilized by sufficiently compliant walls, in particular for spanwise wavelengths large enough. For even larger wavelengths, a spanwise-periodic hydroelastic wave precedes the onset of the streamwise vortex instability.

This brief overview shows the richness of the results obtained during the past 50 years on the interaction between a flow and a compliant wall. It also appears that the influence of the compliant walls on the flow is very complex and highly dependent on the configuration. As a consequence, for many common wall-bounded configurations, the influence of compliant walls on the stability of the base motion is still unknown. This is notably the case when the fluid is bounded by two infinitely long coaxial cylinders and dragged by the rotation of one (or both) cylinder. The configuration has important technological applications, for example in the paper industry for the flow between two adjoining rollers in a printing press. As in the curved-channel case, the Taylor–Couette flow is subjected to a centrifugal instability mechanism promoting the appearance of contra-rotative toroidal vortices known as Taylor vortices. This configuration has been widely studied when the walls are rigid since the pioneering works of Mallock (1888, 1896), Couette (1890) and Taylor (1923) a few years later. However, to the authors' knowledge, only two studies have briefly considered the compliant Taylor–Couette flow. The first study, presented at two APS Meetings by Kempf & McHugh (1996, 1998), considers the linear stability of axisymmetric modes in the narrow-gap approximation. Both cylinders rotate but only the outer one is assumed to be elastic and governed by Navier's equations. In addition to the centrifugal instability, a hydroelastic mode is identified. For very small speed ratios (ratio between the inner and outer cylinders velocities), the Taylor modes are stabilized by the presence of the outer elastic layer while, for large speed ratios, they are more unstable than those in the rigid-wall case. Moreover, the flow is always unstable to the hydroelastic mode. The second study, by Koga and Nagata, is briefly reported in the book by Carpenter & Pedley (2003). Also in this latter work, both cylinders rotate and only the outer one is compliant, modelled along the lines proposed by Carpenter & Garrad (1985). The linear stability analysis in the narrow-gap approximation shows that compliance increases the range of parameters for which the centrifugal instability is observed. Furthermore, for very compliant walls, the flow instability is initiated by non-axisymmetric hydroelastic modes. These results are interesting but can only be considered preliminary, since very few details are provided. As will be shown here, the Taylor–Couette flow with compliant walls is very complex and a detailed parametric investigation is in order.

The purpose of the present work is to consider the influence of compliance on the stability of a Taylor–Couette configuration in the narrow-gap limit, when only the inner cylinder rotates. In § 2, the formulation of the linear stability problem is given, by using the same approach as adopted by Guaus & Bottaro (2007) for the curved channel. This implies to separately model the behaviour of the flow and of the compliant walls, then to couple them at the interface by suitable boundary conditions. For the sake of clarity, the results have been divided depending on the invariance broken by the perturbations. Sections 3 and 4 are dedicated to axisymmetric modes, which are known to be the most unstable when the walls are rigid and § 5 is dedicated to non-axisymmetric modes, a case which appears to be of particular interest when the walls are soft. Summarising remarks are provided in § 6.

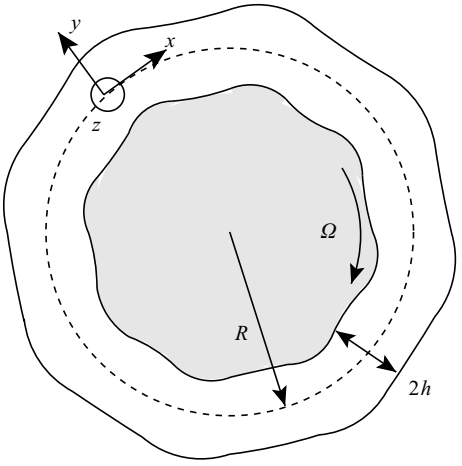

FIGURE 1. Sketch of the configuration in the (x, y) plane.

2. Formulation and governing equations

2.1. *Mean flow and perturbations*

The growth of three-dimensional disturbances riding on top of a steady incompressible base flow in the gap between co-axial differentially rotating infinite cylinders is considered. The Newtonian fluid of kinematic viscosity ν and density ρ is set into motion by the rotation of the inner cylinder at angular velocity Ω while the outer cylinder is fixed (figure 1). The usual Taylor–Couette instability occurs because of an unbalance between viscous and centrifugal forces. Here, since both walls can deform under pressure forces, flow-induced surface waves can propagate and interact with hydrodynamic waves.

A small curvature parameter $\gamma = 2h/R$ is assumed, where $2h$ is the distance between the walls when they are undeformed and R is the constant radius of curvature at the gap centreline. Since γ is small, it is convenient to work with a set of 'pseudo-Cartesian' dimensionless coordinates (x, y, z), defined from the cylindrical coordinates (θ, r, ξ), which read

$$x = \frac{R\theta}{h} = \frac{2\theta}{\gamma}, \quad y = \frac{r-R}{h} = \frac{2(r-R)}{\gamma R}, \quad z = \frac{\xi}{h} = \frac{2\xi}{\gamma R}.$$

The azimuthal, radial and axial components of the velocity (U_θ, U_r, U_ξ) are written in terms of the streamwise, normal and spanwise components (U, V, W), respectively. Here, velocity vector and pressure are made dimensionless with $U^* = R\Omega$ and ρU^{*2}. Each non-dimensional quantity $\tilde{\boldsymbol{Q}} = (\tilde{U}, \tilde{V}, \tilde{W}, \tilde{P})^{\mathrm{T}}$ is decomposed into a mean steady part $\boldsymbol{Q}(x, y) = (U, 0, 0, P)^{\mathrm{T}}$ and a fluctuation $\boldsymbol{q}(x, y, z, t) = (u, v, w, p)^{\mathrm{T}}$.

The mean flow solution is obtained from the Navier–Stokes equations in cylindrical coordinates and, after transformation into the pseudo-Cartesian system, it is found at second order in γ that the azimuthal velocity distribution reads

$$U(y) = \frac{1-y}{2} + \frac{\gamma}{2}\left(-\frac{3}{4} + \frac{y}{2} + \frac{y^2}{4}\right) + \frac{\gamma^2}{16}\, y\,(1-y^2). \tag{2.1}$$

The linearized mean velocity solution and all the following linearized equations are truncated to second order in γ because the curvature effect appears as a term proportional to γ^2 in the compliant shells model (see (2.5) in § 2.3).

2.2. *Linear stability equations*

The equations of motion for the flow perturbation are obtained in two steps. First, the Navier–Stokes equations written for the cylindrical variables (u_θ, u_r, u_ξ, p^*) are linearized about the mean flow. Then, this set of equations is written in the (x, y, z) coordinate system up to second order in γ, leading to

$$\begin{aligned} m_1\frac{\partial u}{\partial x}+\frac{\partial v}{\partial y}+\frac{\partial w}{\partial z}+m_2 v &= 0,\\ u_t+m_1U\frac{\partial u}{\partial x}+(U'+m_2U)v &= -m_1\frac{\partial p}{\partial x}+\frac{1}{Re}\left(L(u)+m_3\frac{\partial v}{\partial x}-\frac{\gamma^2}{4}u\right),\\ v_t+m_1U\frac{\partial v}{\partial x}-2m_2Uu &= -\frac{\partial p}{\partial y}+\frac{1}{Re}\left(L(v)-m_3\frac{\partial u}{\partial x}-\frac{\gamma^2}{4}v\right),\\ w_t+m_1U\frac{\partial w}{\partial x} &= -\frac{\partial p}{\partial z}+\frac{1}{Re}L(w), \end{aligned} \tag{2.2}$$

where the subscript t denotes derivative with respect to time. The metric functions m_i and the operator L are formulated in the Appendix. Strictly speaking, equations given above are not $\mathcal{O}(\gamma^2)$ since terms like m_1U or m_2U contain terms proportional to both γ^3 and γ^4, given (2.1). Terms of order γ^3 or γ^4 are henceforth neglected. The non-dimensional parameter $Re=\Omega R h/\nu$ is the Reynolds number. Although for the Taylor–Couette problem it is customary to work by using the Taylor number Ta (defined as $Ta=64\,\Omega^2h^4/\nu^2$), we prefer here to maintain the Reynolds number as a working parameter to assess the relevance of Taylor and hydroelastic modes in the general case of three-dimensional disturbances. The Taylor number can then be easily recovered from the relation $Ta=16\,(\gamma\ Re)^2$.

Small three-dimensional space and time-periodic flow perturbations are considered in the form

$$\boldsymbol{q}(x, y, z, t)=\hat{\boldsymbol{q}}(y)\exp[\mathrm{i}(\alpha x+\beta z)+\sigma t], \tag{2.3}$$

where the real numbers α and β are, respectively, the azimuthal and axial wavenumbers and $\sigma=\sigma_r+\mathrm{i}\sigma_i$ is a complex number. Its imaginary part is the frequency and its real part σ_r is the growth rate of the wave. Due to the periodicity of the configuration, the azimuthal wavenumber in the original cylindrical coordinate system is an integer. However, the choice of an integer value in the pseudo-Cartesian system would not guarantee an exactly periodic configuration (in the complete cylindrical system), since small terms have been neglected. To make things simple, we choose a dimensionless azimuthal wavenumber α proportional to an integer n via the relation $\alpha=n\gamma/2$ in the pseudo-Cartesian system, keeping in mind that conclusions for non-integer values can be easily interpolated from the results provided. Introducing (2.3) into (2.2) produces a generalized eigenvalue problem of the form $\mathscr{A}\hat{\boldsymbol{q}}=\sigma\mathscr{B}\hat{\boldsymbol{q}}$, where $\hat{\boldsymbol{q}}=(\hat{u}\ \hat{v}\ \hat{w}\ \hat{p})^{\mathrm{T}}$ is the eigenvector.

2.3. *Compliant wall model*

The compliant walls are modelled as spring-backed cylindrical shells, following the lead of Carpenter & Garrad (1985) for an isotropic thin compliant plate. A sketch of the model is drawn in figure 2. The walls are composed of flexible thin cylindrical shells supported by rigid frames through arrays of springs and dampers. They are constrained to move only in the y normal direction and only under flow pressure fluctuations, the contribution of the normal viscous stresses being negligible (Ehrenstein & Rossi 1996). Asterisks in the following equation denote dimensional

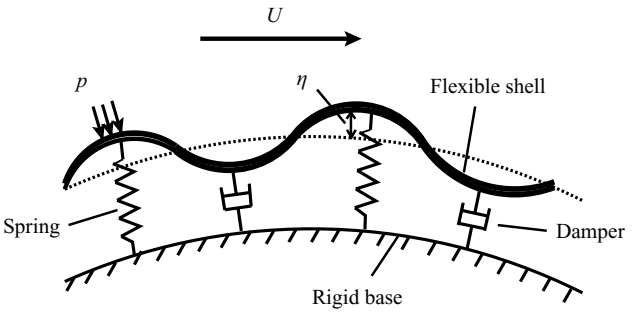

FIGURE 2. Isotropic surface-based model for a compliant shell.

quantities and η^* is the normal displacement of each wall from its equilibrium position. The equation of motion of each curved compliant surface can be obtained from Love's thin cylindrical shell theory (Timoshenko & Woinowsky-Krieger 1959)

$$\left[\left(m^*\frac{\partial^2}{\partial t^{*2}}+d^*\frac{\partial}{\partial t^*}+B^*\Delta_h^{*2}-T^*\Delta_h^*+K^*\right)\Delta_h^{*2}+\frac{E^*H}{R^2}\frac{\partial^4}{\partial z^{*4}}\right]\eta^*=\begin{cases}\Delta_h^{*2}p^*(h)\\-\Delta_h^{*2}p^*(-h)\end{cases}, \tag{2.4}$$

with $\Delta_h^*=\partial^2/\partial x^{*2}+\partial^2/\partial z^{*2}$. In this equation, m^* is the plate mass per unit area, d^* is the wall damping coefficient, $B^*=E^*H/[12(1-\hat{\nu}^2)]$ is the flexural rigidity of the shell, with E^* Young modulus, H shell thickness and $\hat{\nu}$ Poisson's coefficient; K^* is the spring stiffness per unit width and T^* is the longitudinal tension per unit width. The term on the right-hand side represents the normal stress exerted by the fluid on the shell with p^* the flow pressure fluctuation. Koga and Nagata use the same wall model as (2.4) in their study of the Taylor–Couette flow between compliant cylinders (see Carpenter & Pedley 2003).

In scaling the wall properties, it is important to adopt reference quantities such that the non-dimensional wall parameters vary independently from the non-dimensional flow properties, particularly the Reynolds number. Thus, we impose that variations on Re are only related to changes in the angular velocity Ω and scale the wall properties with the fixed quantities h, ρ and ν related to the fluid and the geometry as

$$m=\frac{m^*}{\rho h},\quad d=\frac{d^*h}{\rho\nu},\quad B=\frac{B^*}{\rho\nu^2h},\quad E=\frac{E^*h^2}{\rho\nu^2},\quad K=\frac{K^*h^3}{\rho\nu^2},\quad T=\frac{T^*h}{\rho\nu^2}.$$

After writing the wall displacement, scaled by h, as a normal mode in the form

$$\eta=\hat{\eta}\exp[\mathrm{i}(\alpha x+\beta z)+\sigma t],$$

a dimensionless shell displacement equation is obtained

$$\left[m\sigma^2+\frac{d}{Re}\sigma+\frac{1}{Re^2}\left(Bk^4+Tk^2+K+\frac{H}{h}\frac{\gamma^2}{4}E\frac{\beta^4}{k^4}\right)\right]\hat{\eta}=\begin{cases}\hat{p}(1)\\-\hat{p}(-1)\end{cases}, \tag{2.5}$$

with $k^2=\alpha^2+\beta^2$. Compared to the displacement equation for a thin plate (Carpenter & Garrad 1985) an additional term proportional to γ^2 introduces two new parameters, the ratio H/h and the dimensionless Young modulus E related to the dimensionless flexural rigidity by

$$E=12(1-\hat{\nu}^2)\left(\frac{h}{H}\right)^3B.$$

For the compliant materials used in typical experiments (silicon or natural rubber), the Poisson's coefficient is close to 0.5 (Buckingham, Hall & Chun 1985; Joslin, Morris & Carpenter 1991; Carpenter 1993), and thus we set $\hat{\nu}=0.5$. Then, the only new parameter compared to the plane-wall case is the ratio H/h.

2.4. *Boundary conditions coupling*

The boundary conditions impose the continuity of velocity at the displaced interface between the solid and fluid parts; for the outer wall at $y=1+\eta$ we have

$$U+u=0, \quad v=\eta_t, \quad w=0,$$

and linearization around $y=1$ yields

$$\hat{u} \; + \; \hat{\eta}\,U'=0, \quad \hat{v}-\sigma\,\hat{\eta}=0, \quad \hat{w}=0.$$

The displacement $\hat{\eta}$ can be eliminated to get a simpler hydrodynamic boundary condition

$$\sigma\hat{u}+U'\hat{v}=0. \tag{2.6}$$

Likewise, the compliant model equation (2.5) becomes for $y=+1$

$$m\sigma\hat{v}+\frac{d}{Re}\hat{v}-\frac{1}{U'Re^2}\left(Bk^4+K+Tk^2+\frac{H}{h}\frac{\gamma^2}{4}E\frac{\beta^4}{k^4}\right)\hat{u}=\hat{p}. \tag{2.7}$$

Hence, the three boundary conditions for $y=1$ are $\hat{w}=0$ and (2.6) and (2.7). For the inner wall at $y=-1$, the same set of equations applies, except for the sign in front of the pressure term in (2.7). With these six boundary conditions the generalized eigenvalue problem can be solved.

2.5. *Energy balance for the fluid–walls system*

The energy balance for the fluid–walls system is analysed through a modified version of Reynolds–Orr energy equation. The time derivative of the disturbance fluid kinetic energy E_k^f is obtained by accounting for the inhomogeneous boundary conditions in the Reynolds–Orr equation (Guaus & Bottaro 2007)

$$\overbrace{\left(\int_{-1}^{1}\frac{\overline{u_iu_i}}{2}\,\mathrm{d}y\right)_t}^{\left(E_k^f\right)_t}=-\int_{-1}^{1}U'\overline{uv}\,\mathrm{d}y\;-\;\frac{1}{Re}\int_{-1}^{1}\overline{\frac{\partial u_i}{\partial x_j}\frac{\partial u_i}{\partial x_j}}\,\mathrm{d}y+\int_{-1}^{1}m_2U\overline{uv}\,\mathrm{d}y$$
$$-\int_{-1}^{1}m_2\overline{pv}\,\mathrm{d}y+\frac{1}{Re}\int_{-1}^{1}\left(m_4\overline{\frac{\partial u_i}{\partial x}\frac{\partial u_i}{\partial x}}+m_3\left(\overline{u\frac{\partial v}{\partial x}}-\overline{v\frac{\partial u}{\partial x}}\right)\right)\mathrm{d}y$$
$$-\frac{\gamma^2}{8}\int_{-1}^{1}(\overline{u^2}+\overline{v^2}-\overline{w^2})\,\mathrm{d}y\;-\;\overline{vp}\Big|_{-1}^{1}+\frac{1}{Re}\left(\overline{u\frac{\partial u}{\partial y}}+\overline{v\frac{\partial v}{\partial y}}\right)\Big|_{-1}^{1}+\frac{m_2}{Re}\frac{\overline{u^2}+\overline{v^2}}{2}\Big|_{-1}^{1}.$$

In this equation, the repeated Einstein convention has been employed and overbars denote averaging over a period along x and z. A similar kinetic energy equation was derived by Domaradzki & Metcalfe (1987) and Carpenter & Morris (1990) for the case of the temporal development of two-dimensional disturbances in a boundary layer over a compliant wall. For the case of spatially developing TS waves in a plane channel with finite compliant panels, the energy equation was given by Davies & Carpenter (1997*b*).

Following the lead of Hoepffner, Bottaro & Favier (submitted), the term $\overline{vp}\,|_{-1}^{1}$ is rewritten to introduce the wall kinetic and potential energies E_k^w and E_p^w

$$\overline{vp}\,\big|_{-1}^{1} = \sum_{-1}^{1}\left[\underbrace{m\left(\frac{\overline{\eta_t^2}}{2}\right)_t}_{(E_k^w)_t} + \underbrace{\frac{d}{Re}\overline{\eta_t^2}}_{\text{wall damping}} + \underbrace{\frac{1}{Re^2}\left(B\Delta_h^2 + T\Delta_h + K + \frac{H}{h}\frac{\gamma^2}{4}E\right)\left(\frac{\overline{\eta^2}}{2}\right)_t}_{(E_p^w)_t}\right].$$

The total perturbation energy of the flow-walls system can thus be defined as

$$E = \underbrace{E_k^f}_{flow} + \underbrace{\sum_{-1}^{1}\left(E_k^w + E_p^w\right)}_{walls}. \tag{2.8}$$

and the total energy budget reads

$$\begin{aligned} E_t = {} & \overbrace{-\int_{-1}^{1} U'\overline{uv}\,\mathrm{d}y}^{(I_1)} \overbrace{-\frac{1}{Re}\int_{-1}^{1}\overline{\frac{\partial u_i}{\partial x_j}\frac{\partial u_i}{\partial x_j}}\,\mathrm{d}y}^{(I_2)} + \overbrace{\int_{-1}^{1} m_2 U\overline{uv}\,\mathrm{d}y}^{(G_1)} \\ & \underbrace{-\int_{-1}^{1} m_2\overline{pv}\,\mathrm{d}y}_{(G_2)} + \underbrace{\frac{1}{Re}\int_{-1}^{1}\left(m_4\overline{\frac{\partial u_i}{\partial x}\frac{\partial u_i}{\partial x}} + m_3\left(\overline{u\frac{\partial v}{\partial x}} - \overline{v\frac{\partial u}{\partial x}}\right)\right)\mathrm{d}y}_{(G_3)} \\ & \underbrace{-\frac{\gamma^2}{8}\int_{-1}^{1}(\overline{u^2} + \overline{v^2} - \overline{w^2})\,\mathrm{d}y}_{(G_4)} \underbrace{-\sum_{-1}^{1}\left[\frac{d}{Re}\overline{\eta_t^2}\right]}_{(C_1)} + \underbrace{\frac{1}{Re}\left(\overline{u\frac{\partial u}{\partial y}} + \overline{v\frac{\partial v}{\partial y}}\right)\Big|_{-1}^{1}}_{(C_2)} + \underbrace{\frac{m_2}{Re}\frac{\overline{u^2} + \overline{v^2}}{2}\Big|_{-1}^{1}}_{(C_3)}. \end{aligned} \tag{2.9}$$

The terms (I_1) and (I_2) are, respectively, the Reynolds stress production and dissipation terms. The additional terms in (2.9) are related to our specific configuration: the terms (G_1), (G_2), (G_3), (G_4) and (C_3) arise from the curvature of the walls while the terms (C_1), (C_2) (and (C_3)) arise from their movement. Extensive numerical results indicate that only the terms (C_1), (C_2) and (G_1) are significant in the disturbance energy balance, the remaining terms being invariably negligible. The term (C_1) represents the viscous damping in the walls; (C_2) is the rate of irreversible work done to the wall by fluctuations in viscous stresses and (G_1) is the energy exchange between the mean flow and the perturbation arising because of the curvature of the walls. The curvature effect is intrinsically included in all terms. For example, in (I_1) curvature is explicitly present in the mean profile and, in the terms (I_2), (C_1) and (C_2), curvature modifies the normal shape of the perturbation profile implicitly. The detailed contribution of the different terms to the disturbance energy balance will be discussed further.

3. Axisymmetric perturbations ($n = 0$)

3.1. *Numerical implementation and validation*

The generalized eigenvalue system with all the boundary conditions has been discretized using a Chebyschev collocation method. The spectrum of eigenvalues has been explored by employing both global (QZ) and local (Arnoldi) techniques in a

Matlab code previously validated for the case of a plane channel flow with compliant walls (Guaus & Bottaro 2007). We have also checked the results against those for the Taylor–Couette configuration with rigid walls (Chandrasekhar 1981; Drazin & Reid 1981) by considering the limit $B \to \infty$, always verifying that the eigenvalues σ of interest were converged to several significant digits.

The number of parameters at play is very large; hence we have restricted attention to the case of two walls with identical physical and mechanical properties. We have chosen to concentrate on the influence of three wall parameters: the flexural rigidity B, the spring stiffness K and the damping coefficient d; the mass of each wall is arbitrarily fixed to $m = 2$ and the longitudinal tension T is assumed equal to zero throughout. The ratio H/h between the thickness of the walls and the gap height is also chosen constant and equal to 1 for simplicity. Finally, we have to set the curvature parameter by choosing $\gamma = 0.0174$ as in the rigid-walls experiments by Prigent & Dauchot (2000).

The effect of the untensioned-wall assumption on the complex wave velocity can be seen from the wall model (2.5) in the case of natural oscillation, i.e. in the absence of fluid. Neglecting the damping coefficient, the complex phase velocity is

$$\tilde{c} = \frac{\sigma}{k} = \frac{\mathrm{i}}{Re\sqrt{m}}\sqrt{Bk^2 + T + \frac{K}{k^2} + \frac{H}{h}\frac{\gamma^2}{4}E\frac{\beta^4}{k^6}}.$$

In the limit of infinite wavelength ($k \to 0$), the velocity is proportional to $1/k$ while in the limit of small wavelength ($k \to \infty$), the velocity is proportional to k. The derivative of the modulus of the phase velocity with respect to the tension force is in the range $[10^{-3}, 10^{-8}]$ using the numerical parameters of our study. Thus, the tension T plays a minor role and can be neglected.

When fluid is present, its effect on the compliant surfaces can be approximated by the presence of an added mass m_a. In the analysis by Hoepffner *et al.* (submitted), such an added mass takes a different form in the case of sinuous or varicose streamwise-homogeneous wall waves in a channel. In the present configuration, there are no waves with exact sinuous or varicose symmetry, but results to be shown indicate that quasi-sinuous and quasi-varicose axisymmetric waves appear. Empirical arguments developed by Hoepffner *et al.* (submitted) suggest to take $m_a = (1 - \mathrm{e}^{-\beta})/\beta$ for the sinuous-like waves and $m_a = (1 - \mathrm{e}^{-\beta})/\beta + 1/\beta^2$ for the varicose-like waves, so that $\tilde{c}$ can be approximated by

$$\tilde{c} = \frac{\sigma}{k} = \frac{\mathrm{i}}{Re\sqrt{m + m_a}}\sqrt{Bk^2 + T + \frac{K}{k^2} + \frac{H}{h}\frac{\gamma^2}{4}E\frac{\beta^4}{k^6}}.$$

Here, the accuracy of such an approximation will be assessed by comparison with the full numerical results.

3.2. *Features of the axisymmetric hydroelastic modes*

When the walls are compliant, four new modes appear in addition to the classical centrifugal modes present in the rigid-wall case. Here, these modes driven by the wall flexibility are termed hydroelastic modes or FISI for flow-induced surface instabilities. They are clearly identified in figure 3(*a*) by comparing the spectra in the rigid and compliant cases for a Reynolds number fixed at $Re = 250$ and an axial wavenumber $\beta = 1$. The rigid-wall spectrum presents the classical centrifugal eigenvalues with zero phase velocities. For the chosen set of parameters, only one centrifugal mode is unstable and corresponds to the appearance of Taylor vortices.

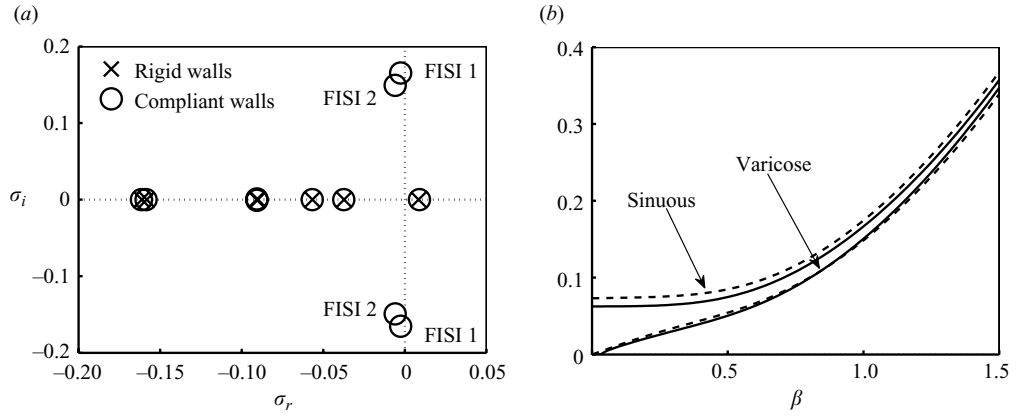

FIGURE 3. (*a*) Comparison of the axisymmetric eigenvalue spectrum for the rigid-wall and compliant-wall cases for $\beta = 1$ and $Re = 250$. The hydroelastic modes are labelled FISI. (*b*) Frequency of the sinuous-like and varicose-like axisymmetric FISI modes (solid lines) compared to the results obtained using the added mass model (dashed lines) for $Re = 250$. The wall parameters are $B = 4000$, $K = B/4$ and $d = 0$.

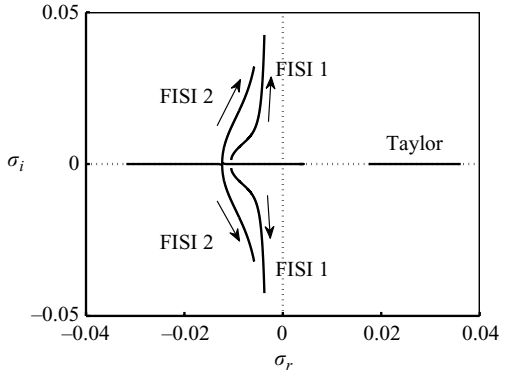

FIGURE 4. Evolution of the main axisymmetric eigenvalues with the spanwise wavenumber ($0.2 \leqslant \beta \leqslant 2$). The parameters are $Re = 250$, $B = 400$, $K = B/16$ and $d = 0$. Arrows denote increasing β.

In the compliant-wall case, the four hydroelastic modes are stable and are coupled in pairs (i.e. they are pairs of complex conjugate modes), which means that their superposition can yield a standing wave. The two modes labelled FISI 1 are sinuous-like modes and the two modes labelled FISI 2 are varicose-like modes. Their frequencies are compared to those obtained using the added mass model in figure 3(*b*) with a satisfactory quantitative agreement.

For relatively large axial wavenumbers, such as $\beta = 1$ in figure 3(*a*), the hydroelastic modes remain stable and coupled by pairs for all wall parameters considered. The analysis of spectra highlights that the most interesting behaviour of hydroelastic modes occurs for axial wavenumbers small enough: for sufficiently soft walls, when β decreases, the FISI modes become stationary and, once stationary, possibly unstable. This is illustrated in figure 4, in which we have fixed $Re = 250$, $B = 400$, $K = B/16$ and $d = 0$, and spanned the β range from 0.2 to 1. This figure has to be looked at together with figure 5 where the real (growth rate) and imaginary (frequency) parts of σ versus

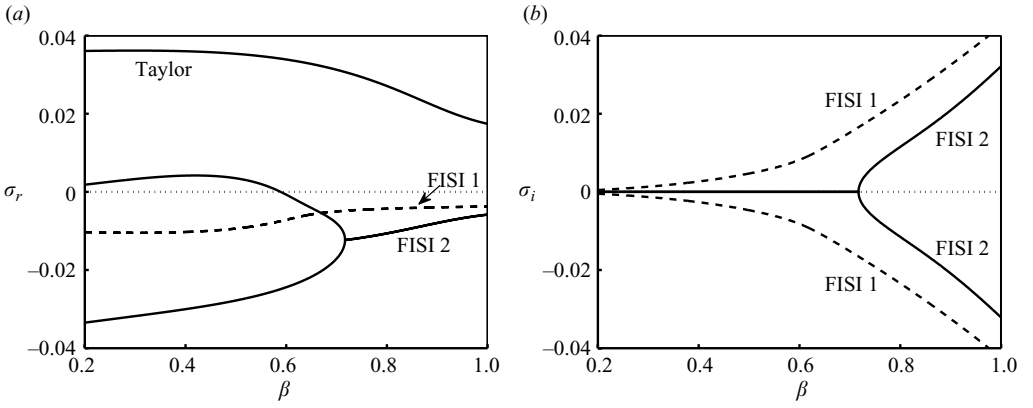

FIGURE 5. Real (a) and imaginary parts (b) of σ versus β. Same parameters as in figure 4. In (b), the zero frequency of the centrifugal mode is not shown.

β are separately presented. For $\beta > 0.71$, the spanwise phase velocity $|\sigma_i/\beta|$ of the four hydroelastic modes decreases with β until the phase velocity of FISI 2 reaches zero for $\beta = 0.71$. For $\beta < 0.71$, the two FISI 2 modes have zero phase velocities and growth rates evolving in opposite directions when β decreases. Each FISI 2 mode is then associated with a static normal displacement of the walls since their frequency is zero ($\sigma_i = 0$). Hence, a hydroelastic instability occurs for $\beta < 0.59$ as a static wall deformation growing exponentially in time. The FISI 1 modes, which remain stable, are subject to a similar behaviour for $\beta < 0.12$ (not shown). For the whole β range, however, the most unstable mode is always a centrifugal, Taylor mode.

For the parameters chosen in figures 4 and 5, the phenomenon of intersection of two FISI 2 branches on the real axis is observed; for other sets of parameters, an intersection can occur between a real FISI eigenvalue whose growth rate decreases (or increases) with β and another eigenvalue whose growth rate behaves in the opposite way. Section 3.6 is dedicated to the implications of these intersections between branches.

3.3. *Influence of wall parameters*

The effect of varying the parameters K and B on the neutral curves can be assessed from figure 6, in the absence of damping. As can be inferred from the spectral analysis in the previous section, wall compliance does not modify the flow stability properties at large axial wavenumbers where a Taylor mode always dominates. At small axial wavenumbers ($\beta \lesssim 1.5$ for $B = 400$ and $\beta \lesssim 1$ for $B = 4000$), the range of unstable wavelengths for a given Reynolds number increases with wall flexibility (i.e. when K and B decrease). Different instability thresholds exist depending on K and B and the critical Reynolds number is significantly reduced, compared to the rigid-wall value, in the case of walls which are sufficiently soft (figure 6a). Furthermore, for very soft walls ($B = 400$ and $K = B/16$ for instance), numerical results obtained for decreasing values of β suggest that the critical axial wavenumber tends to zero, which would correspond to a perturbation with no axial structure. The degeneracy of the equations in the limit $\alpha = 0$, $\beta \to 0$ has been examined in an asymptotic analysis described succinctly in § 4. This degenerate behaviour for $\beta \to 0$ has also been observed by Guaus & Bottaro (2007) in the curved-channel configuration, and explored in details by Guaus (2008).

Until now, the ideal situation with no internal wall damping has been considered. However, many studies on wall compliance have demonstrated the large influence

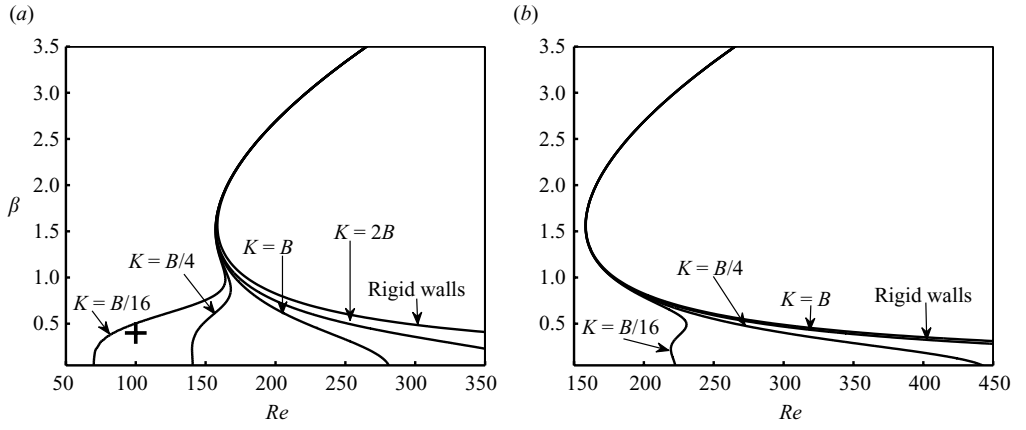

FIGURE 6. Neutral curves showing the influence of the spring stiffness K on axisymmetric perturbations with (a) $B = 400$ and (b) $B = 4000$. In both cases, $d = 0$. The cross in (a) corresponds to $Re = 100$ and $\beta = 0.4$.

of wall damping on flow stability. The effect of introducing a non-zero value of d can be assessed from figure 7 which presents the neutral curves and the curves of constant positive growth rate for the two most unstable modes, considering different wall damping parameters: $d = 0$, 100 and 1000. In addition to the most unstable mode already presented in figure 6, results are plotted for the second most unstable mode (dashed line); it is unstable only for small values of β and grows much more slowly than the most unstable mode (as can be inferred by comparing the spacing between isolines in the two cases).

Compared to B and K, wall damping has a minor impact on flow stability. Introducing damping into the walls has very little effect on the appearance of either modes, and neutral curves for different values of d can almost be superposed to one another. The influence of d is only visible for small β's when focusing on isolines of constant positive growth rate σ_r: both modes considered experience a slower amplification when d increases.

3.4. *Structure of the modes*

The structure of the most unstable mode for $\beta = 0.4$ and $Re = 100$ in the case $B = 400$, $K = B/16$ and $d = 0$ is shown in figure 8 and compared with the structure of the least stable mode in the rigid-wall case. These parameters correspond to the point marked with a cross in figure 6(a). Isocontours of the azimuthal velocity u and velocity vectors (v, w) are displayed in the (y, z/λ_z) plane, with $\lambda_z = 2\pi/\beta$ axial wavelength. In the rigid-wall case, the least stable mode presents the classical centrifugal structure, with centrally positioned pairs of contra-rotating vortices. In the compliant-wall case, the most unstable mode has similar structure; however, because of wall flexibility, the contra-rotating vortices are closer to the inner wall ($y = -1$). Moreover, the u velocity presents very high values near the walls.

Figure 8 also shows a sketch of the walls displacements which appears to be strongly linked to the position of the vortices. First, the wall displacement is more important for the inner wall, near which the vortices are located. Moreover, the two vortices induce maximum positive v velocity for $z/\lambda_z = 0.5$. This provokes displacements of the walls, with the outer one pushed away from the flow and the inner one sucked towards the outer one, in a sinuous-like motion.

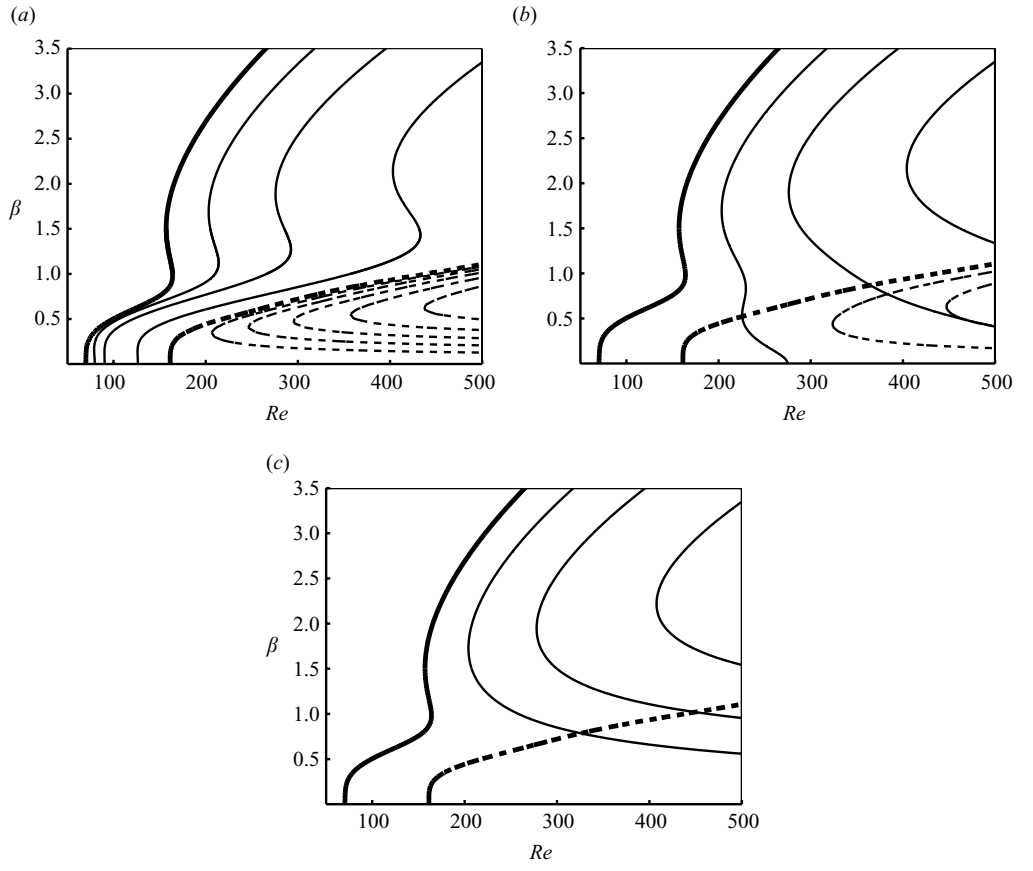

FIGURE 7. Neutral curves (thick lines) and curves of constant positive growth rate for the two most unstable axisymmetric modes with (*a*) $d=0$, (*b*) $d=100$ and (*c*) $d=1000$. The spacing between two adjacent lines is $\Delta\sigma_r = 1\times10^{-4}$ for the solid lines and $\Delta\sigma_r = 2\times10^{-5}$ for the dashed lines. The other wall parameters are $B=400$ and $K=B/16$.

The structure of the hydroelastic FISI 2 mode unstable in figures 4 and 5 is displayed in figure 9 for $\beta=0.4$ in the $(y, z/\lambda_z)$ plane. The mode is characterized by high values of the streamwise velocity at the walls and by a varicose-like form of walls displacement.

3.5. *Energy budget*

In this section, the energy budget of the fluid–walls system for the most unstable axisymmetric modes is analysed. The plot of the growth rate of the disturbance energy E versus β (*a*) and the terms contributing the most to the energy budget (*b*) are presented in figure 10 for the most unstable – centrifugal-like – mode of figure 7(*a*). In figure 10(*a*), only the fluid kinetic energy term is significant in the total energy for the compliant case, the wall energy contribution being negligible. The destabilization of the mode for small wavenumbers, compared to the rigid-wall case, is linked both to an increase of energy production by the Reynolds stresses (I_1) and a decrease of viscous dissipation (I_2) (cf. figure 10*b*).

This is the opposite of what happens for the stabilization of the TS waves in a plane channel (Davies & Carpenter 1997*b*). It is also different from what has been observed by Guaus & Bottaro (2007) for the centrifugal instability in a curved channel. For

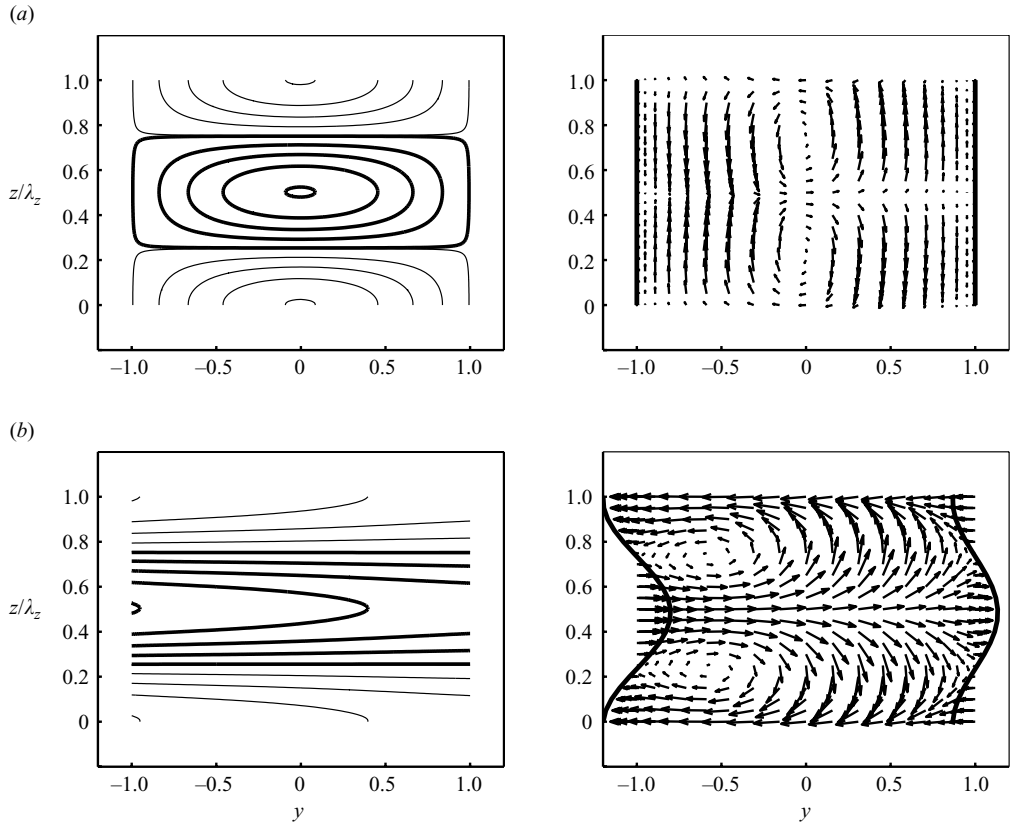

FIGURE 8. Structure of the most unstable axisymmetric mode with $\beta = 0.4$ and $Re = 100$ in the (a) rigid- and (b) compliant-wall cases. (Left) Isocontours of u in the (y, z/λ_z) plane; thick lines: positive isocontours; thin lines: negative isocontours. (Right) Velocity vectors (v, w) in the (y, z/λ_z) plane and sinuous-like wall displacement. In the compliant case, the parameters are $B = 400$, $K = B/16$ and $d = 0$.

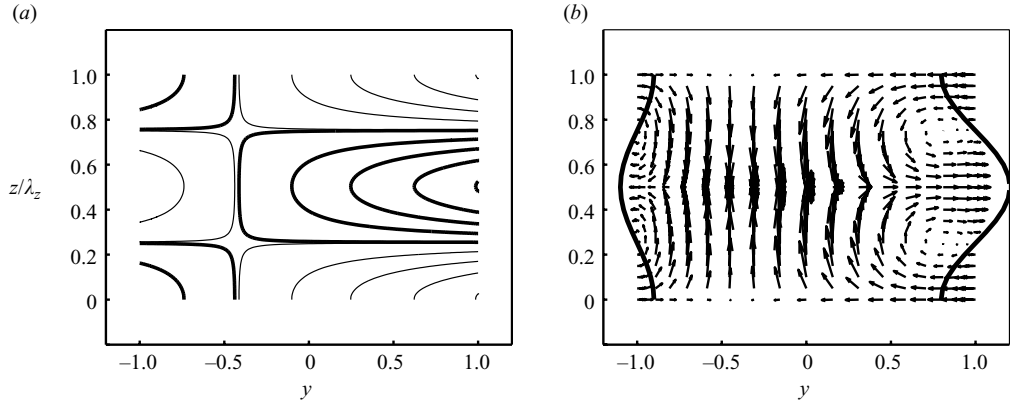

FIGURE 9. Structure of the unstable FISI 2 mode with real eigenvalue shown in figure 4 ($\beta = 0.4$). (a) Isocontours of u in the (y, z/λ_z) plane; thick lines: positive isocontours; thin lines: negative isocontours. (b) Velocity vectors (v, w) in the (y, z/λ_z) plane and varicose-like wall displacement.

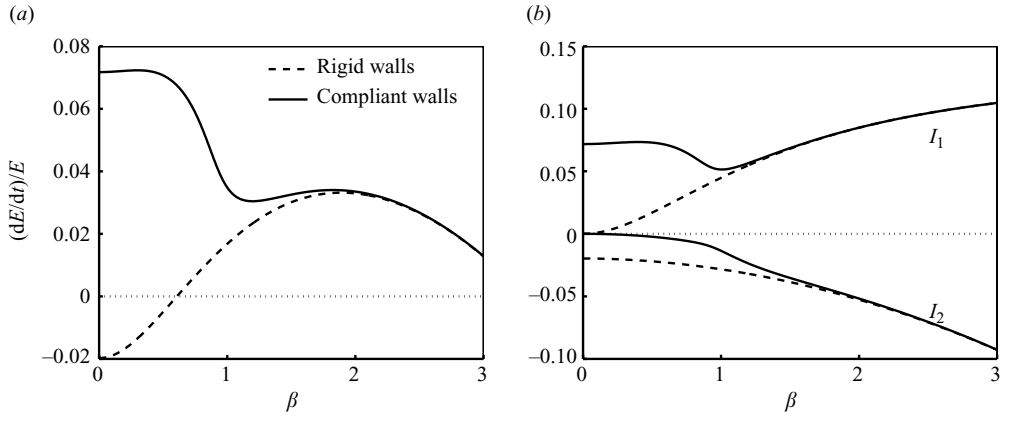

FIGURE 10. (*a*) Disturbance energy growth rate versus spanwise wavenumber ($10^{-3} \leqslant \beta \leqslant 3$) for the most unstable centrifugal-like mode in figure 4. (*b*) Main terms of the disturbance energy balance. All terms are normalized by E. The parameters are $Re = 250$, $B = 400$, $K = B/16$ and $d = 0$.

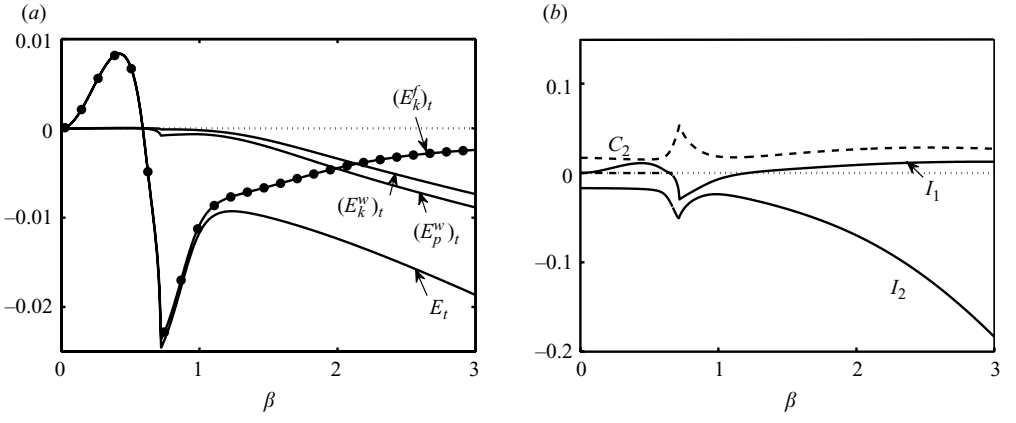

FIGURE 11. (*a*) Disturbance energy growth rate E and its contributing terms (cf. (2.8)) versus spanwise wavenumber ($10^{-3} \leqslant \beta \leqslant 3$) for the FISI 2 mode which becomes unstable in figure 4. The wall energy terms account for both walls. (*b*) Main terms of the disturbance energy balance versus spanwise wavenumber. All terms are normalized by E. The parameters are $Re = 250$, $B = 400$, $K = B/16$ and $d = 0$.

the case of Dean vortices, energetic exchanges with the mean flow remain very small, the destabilization is essentially due to the work done on the wall by the fluctuating viscous stresses (term (C_2)). In the present case, the term (C_2) remains small.

Figure 11 presents the growth rate of the system disturbance energy and its contributing terms (cf. (2.8)) versus β (*a*) for the FISI 2 mode which becomes unstable in figure 4 and the most important terms of the energy balance (*b*). The curves show a break in slope around $\beta = 0.71$, the value for which the imaginary parts of the FISI 2 modes vanish. The destabilization of the disturbance for $\beta < 0.59$ is essentially linked to an increase of the fluid kinetic energy, concentrated near the walls. Both the kinetic and potential wall energy terms have similar evolutions with β. The perturbation is destabilized by energy transfer from the mean flow to the

perturbation ($(I_1) > 0$). For large values of β, the destabilizing influence of (I_1) and (C_2) is compensated by the stabilizing effect of viscous dissipation (I_2).

3.6. *Exchanges between axisymmetric modes with zero phase velocity*

As anticipated at the end of § 3.2, the possible intersections between eigenvalue branches on the real axis, once the frequency of hydroelastic modes vanishes, are now considered. This issue has been isolated in a specific section for the sake of clarity: it provides no direct additional information on modes instability since intersections have been observed to involve only stable modes; nonetheless the phenomenon deserves being mentioned since intersections lead to what we have termed 'exchanges' between modes, that have indirect influence on eigenvalues.

The 'exchange' behaviour is illustrated in figure 12: for the least stable modes, the evolution of the growth rate (left panel) and of the frequency (right panel) are plotted as function of β ($0.2 \leqslant \beta \leqslant 0.8$) for different values of the Reynolds number. For $Re = 200$ and $Re = 185$ (cf. figures 12*a* and 12*b*), the centrifugal (Taylor) mode and the four hydroelastic (FISI) modes are clearly identifiable and the centrifugal mode is always the most unstable one. The FISI 1 modes have conjugate eigenvalues meaning that their phase velocities are opposite. When the Reynolds number decreases, the opposite phase velocities (and therefore the frequency σ_i) of the two FISI 1 modes become close to zero for $\beta \lesssim 0.5$. The FISI 2 modes present the specific behaviour described in § 3.2: they have conjugate eigenvalues for $\beta \gtrsim 0.6$ and real eigenvalues when β decreases. For a Reynolds number larger than $Re = 185$, one of the FISI 2 mode is mildly unstable when $\beta \lesssim 0.4$.

In figure 12(*c*), for $Re = 170$, the situation is more complex:

(1) For $\beta \gtrsim 0.42$, the behaviour of the modes is similar to that at higher Reynolds numbers.

(2) The frequency of the FISI 1 is equal to zero for $0.39 \leqslant \beta \leqslant 0.42$.

(3) For $\beta < 0.39$, one FISI 1 mode and one FISI 2 mode have the same growth rate and opposite phase velocities (dashed lines in figure 12*c*). These modes have similar structures (see further) so that they are indistinguishable from one another.

(4) Above all, the unstable hydroelastic mode, belonging to a FISI 2 branch for $Re = 185$ and $Re = 200$, now belongs to a FISI 1 branch.

In figure 12(*d*), for $Re = 160$, all modes are anew easily identifiable. The two FISI 1 modes and the two FISI 2 modes have again the same behaviour: complex conjugate eigenvalues for large values of β, then real eigenvalues for small ones. However, the unstable hydroelastic mode now belongs to a FISI 1 branch whereas it belonged to a FISI 2 branch at larger Re. This highlights the so-called exchange between a FISI 1 mode and a FISI 2 mode at the moment when their eigenvalues meet on the real axis since on one side and the other of the point of intersection, they have exchanged their behaviours. During the exchange, the structures of the two modes are identical as shown in figure 13 (plot just after the exchange). Similar exchanges between hydrodynamic and surface-based modes have been observed by Levinski, Levy & Cohen (2001) in a linear stability analysis of a compliant wall-jet flow.

A similar exchange, but now between a centrifugal mode and a FISI 2 mode, exists when the Reynolds number is further decreased. For $Re = 110$ (cf. figure 12*e*), the growth rate of the centrifugal mode increases when β is reduced while the growth rate of the hydroelastic modes decreases. However, no exchange occurs because the hydroelastic modes have non-zero frequencies. At $Re = 100$, the centrifugal mode joins a FISI 2 mode with a real eigenvalue for $\beta = 0.5$. For $\beta \leqslant 0.5$, the centrifugal

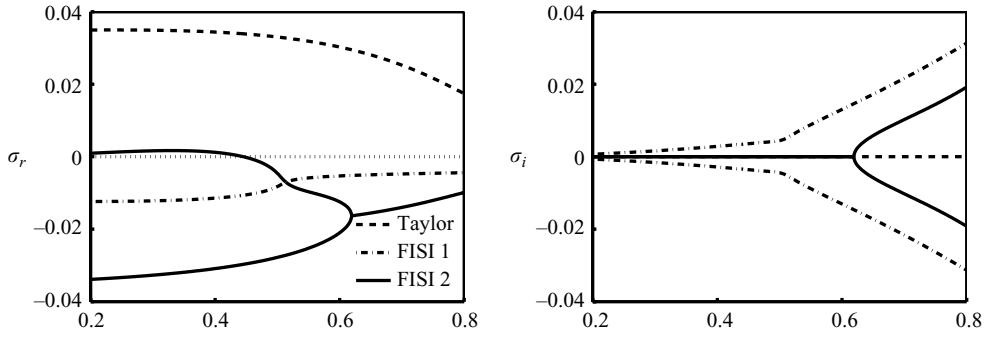

(*a*) *Re* = 200

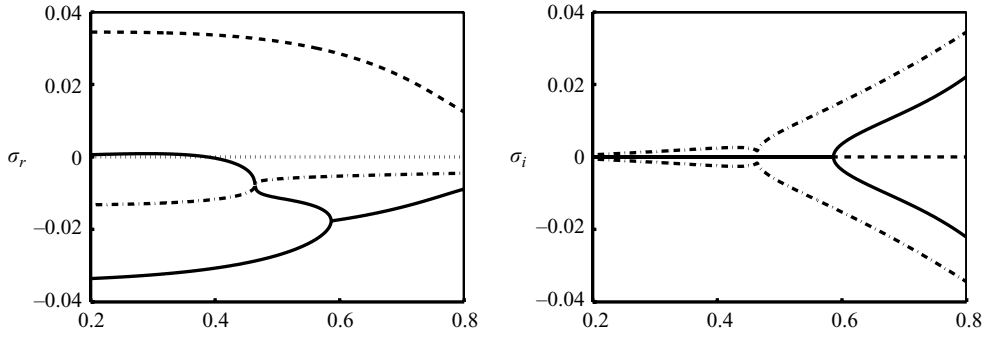

(*b*) *Re* = 185

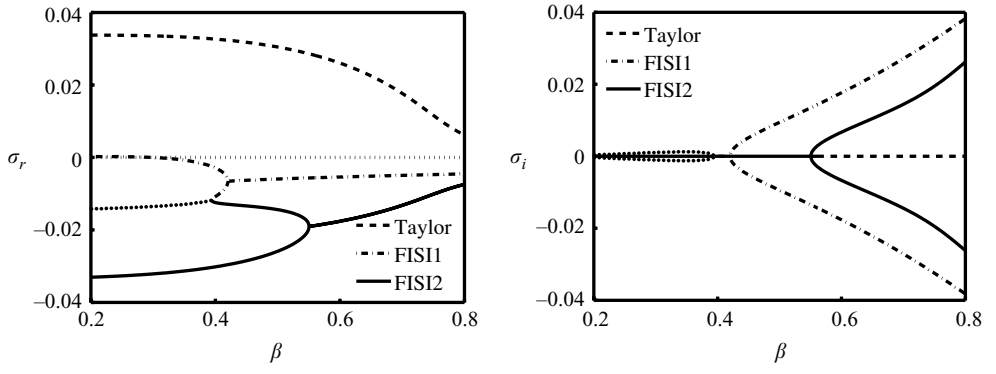

(*c*) *Re* = 170

FIGURE 12. For legend see next page.

and the FISI 2 modes have conjugate eigenvalues (dashed lines in figure 12*f*). The unstable mode for $\beta \leqslant 0.5$ no longer belongs to a centrifugal branch but to a FISI 2 branch. However, as shown in figure 8, the structure of this disturbance still resembles that of a centrifugal mode.

The consequence of these exchanges is that, for small values of β when hydroelastic modes are stationary, it is no longer possible to clearly separate the centrifugal and hydroelastic modes since they belong to different branches, depending on the Reynolds

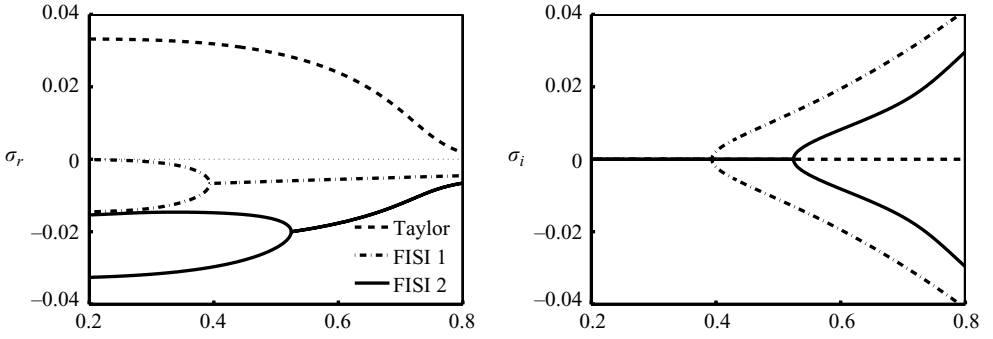

(*d*) $Re = 160$

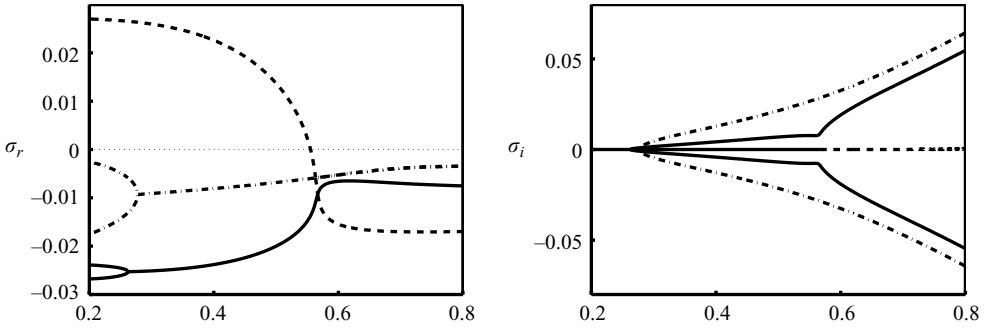

(*e*) $Re = 110$

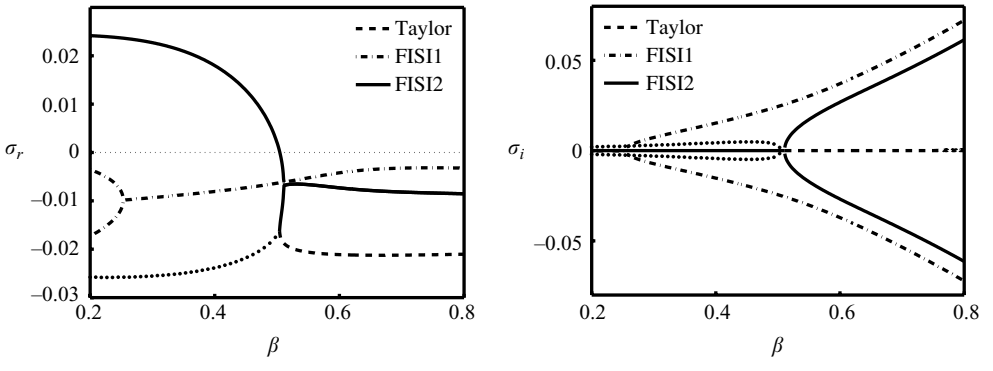

(*f*) $Re = 100$

FIGURE 12. Exchanges between axisymmetric modes with zero phase velocity. Evolution of the main perturbations growth rate (left) and frequency (right) with β ($0.2 \leqslant \beta \leqslant 0.8$) for different values of the Reynolds number. The wall parameters are $B = 400$, $K = B/16$ and $d = 0$. The curves drawn with dotted lines (figures *c* and *f*) correspond to modes which are not clearly identifiable.

number. Then, an unstable eigenvalue can be identified as a FISI or a centrifugal mode if the Reynolds number slightly varies. However, the fact that an unstable mode belongs to one branch or another does not modify its structure. In particular, the most unstable mode at small Reynolds number and low axial wavenumber has

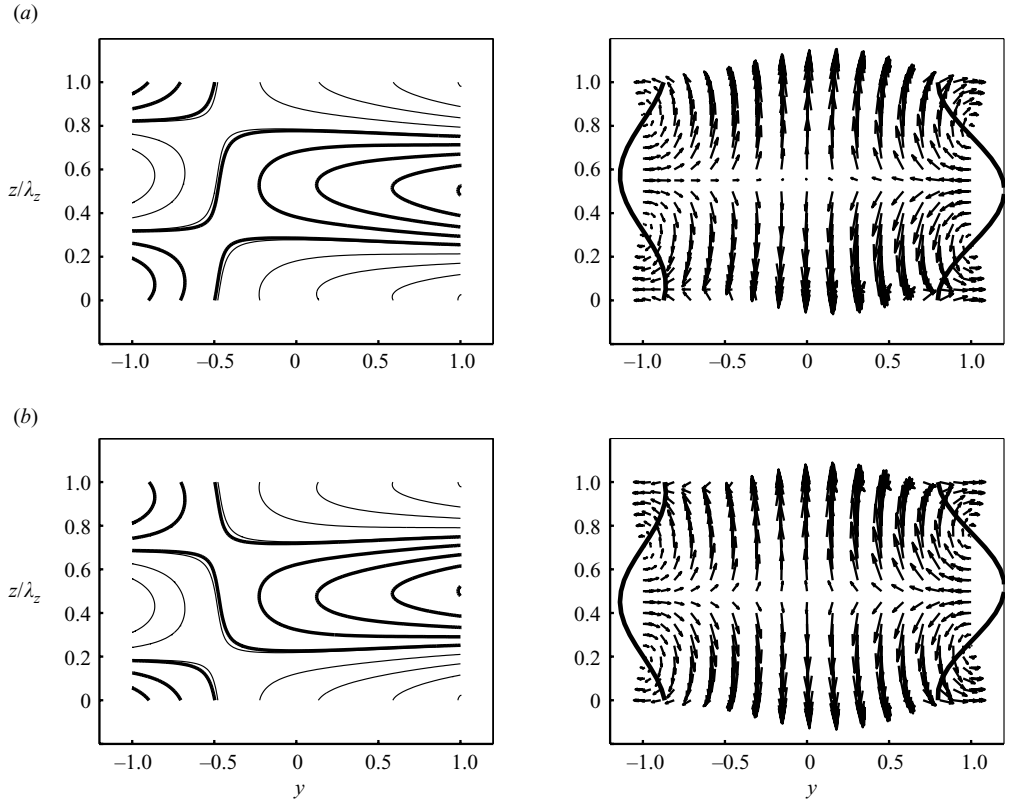

FIGURE 13. Exchange between the FISI 1 and FISI 2 modes with conjugate eigenvalues with $\beta = 0.35$ and $Re = 170$.

the centrifugal structure shown in figure 8. The exchange between stable modes only complicates the linear stability analysis, since it affects modes identification, but does not play a role in the instability mechanism.

3.7. *Preliminary conclusions*

As for the curved-channel configuration (Guaus & Bottaro 2007), the wall compliance has a destabilizing influence on axisymmetric perturbations with small axial wavenumbers compared to the rigid-wall case. In addition to the centrifugal modes already present when the walls are rigid, the flexibility of the walls is responsible for the appearance of four hydroelastic modes whose behaviour strongly depends on the axial wavelength. These four hydroelastic modes are stable for large enough values of β and have opposite phase velocities (pair by pair) which decrease with β. When the walls are very soft, the hydroelastic modes have zero phase velocities and growth rates evolving in opposite ways with β in the limit of vanishing β, possibly yielding a static deformation of the walls. This collision and splitting of the hydroelastic modes on the real axis always occurs when they are stable, contrary to what observed by Argentina & Mahadevan (2005) in their study of fluid-flow-induced flutter in a flag, when instability is observed to arise from a similar collision/splitting effect. Furthermore, unlike what was observed in the curved-channel case, only the stationary axisymmetric hydroelastic modes are possibly unstable here. Finally, interesting exchanges of behaviour between stable steady modes have been observed.

4. Asymptotic analysis for axisymmetric perturbations in the limit of large transverse wavelengths

In this section, an asymptotic analysis, focusing on the degenerate behaviour of axisymmetric disturbances in the large transverse wavelength limit, has been carried out. The study provides little additional understanding on the destabilization mechanisms but interesting information on specific behaviours of the eigenmodes. In particular, the collision/splitting of the hydroelastic (FISI 1) modes on the real axis and the exchanges described in § 3.6 are more methodically described and interpreted then with the numerical calculations.

A solution of the eigenvalue problem is sought through an asymptotic expansion of the eigenmodes in integer power of the small parameters β and γ. The expansion for the eigenvalue σ is written as

$$\begin{aligned}\sigma = {} & \sigma_{00} + \gamma\,\sigma_{01} + \gamma^2\,\sigma_{02} + O(\gamma^3) \\ & + \beta\,(\sigma_{10} + \gamma\,\sigma_{11} + \gamma^2\,\sigma_{12} + O(\gamma^3)) \\ & + \beta^2\,(\sigma_{20} + \gamma\,\sigma_{21} + O(\gamma^2)) + O(\beta^3),\end{aligned}$$

with $\beta \ll 1$ and $\gamma \ll 1$. A similar expression is written for $\hat{\boldsymbol{q}}$; all expressions are then plugged into the equations, and like order terms are collected.

The terms of the expansion calculated are those written above. As far as the eigenvalues are concerned, the following terms have been found to vanish:

$$\sigma_{10} = \sigma_{11} = \sigma_{12} = \sigma_{21} = 0,$$

so that the expression of σ reduces to

$$\sigma = \sigma_{00} + \gamma\sigma_{01} + \gamma^2\sigma_{02} + \beta^2\sigma_{20} + \cdots$$

By considering the eigenvalue problem with $\alpha = \beta = \gamma = 0$, the eigenvalue at order zero can be easily found to be given by

$$\sigma_{00} = \omega_0 \left(-\frac{d}{d_c} + \epsilon\sqrt{\frac{d^2}{d_c^2} - 1} \right) \quad \text{with } \epsilon = \pm 1, \tag{4.1}$$

with

$$d_c = 2\sqrt{K(m+1)} \quad \text{and} \quad \omega_0 = \frac{1}{Re}\sqrt{\frac{K}{m+1}},$$

coherent with the added mass hypothesis of § 3.1. As expected, by considering the wall equation (2.7), the most important wall parameters in the limit $\beta \to 0$ are K, d and m. The real and imaginary parts of the two σ_{00} solutions are plotted versus the damping coefficient d in figure 14(a) with $B = K = 8000$, $m = 2$, $Re = 300$. This set of parameters (for which we have $d_c = 309.8$ and $\omega_0 = 0.172$) will be used in the remainder of the section, in association with $\beta = 0.1$ when numerical results are sought for comparison. The figure shows the behaviour of the σ_{00} eigenvalue as function of wall parameters

(1) When $d = 0$, the two σ_{00} solutions are purely imaginary conjugates, corresponding to neutral perturbations with opposite frequencies $\sigma_i = \epsilon\,\mathrm{i}\,\omega_0$.

(2) When $0 < d < d_c$, the two σ_{00} solutions are complex conjugates. The associated perturbations are stable ($\sigma_r = -\omega_0\,d/d_c$) with opposite phase velocities ($\sigma_i = \epsilon\,i\,\omega_0\sqrt{1 - d^2/d_c^2}$).

(3) Finally, when $d \geqslant d_c$, the two σ_{00} solutions are negative real numbers that generate stable perturbations ($\sigma_r = \omega_0\,(-d/d_c + \epsilon\sqrt{d^2/d_c^2 - 1})$) with zero phase velocities.

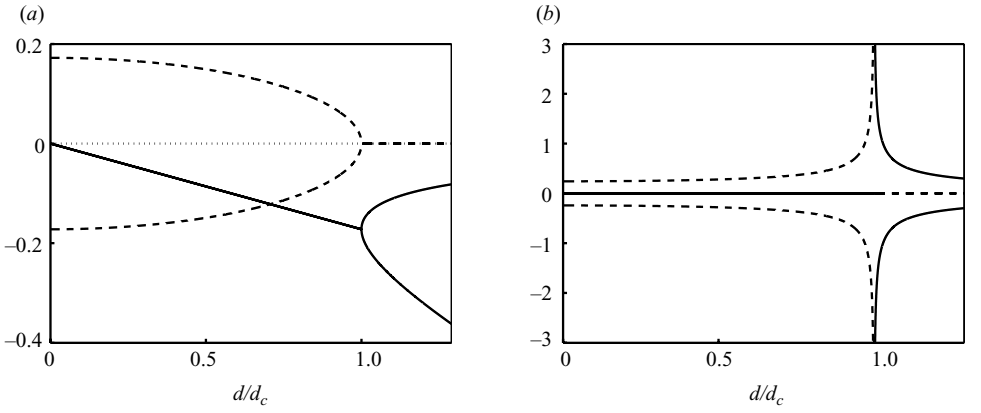

FIGURE 14. Real (solid lines) and imaginary part (dashed lines) of (*a*) σ_{00} and (*b*) σ_{01} versus d/d_c. With the parameters chosen, $d_c = 309.8$.

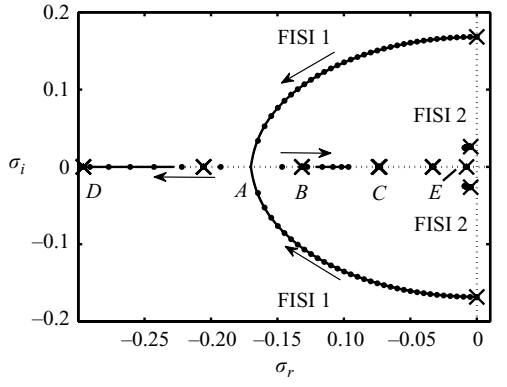

FIGURE 15. Evolution of the numerical eigenvalue spectrum (dots) with d ($0 \leqslant d \leqslant 350$). Comparison with the analytical solution $\sigma_{00}+\gamma\sigma_{01}$ in solid lines ($0 \leqslant d \leqslant 306.2$, $313.2 \leqslant d \leqslant 350$). Crosses mark the numerical eigenvalues for $d = 0$. Arrows denote increasing values of d.

Thus, the two σ_{00} eigenvalues always correspond to stable or marginally stable perturbations.

By proceeding further, it is easy to find the solutions σ_{01}

$$\sigma_{01} = \epsilon \frac{Re}{4\sqrt{d^2 - d_c^2}}.$$

The real and imaginary parts of σ_{01} are plotted in figure 14(*b*) versus d. The solutions present a singularity for $d = d_c$. The two eigenvalues are purely imaginary conjugates for $d < d_c$ and opposite real numbers for $d > d_c$.

The comparison of the numerical spectrum (dots) with the analytical solutions $\sigma_{00}+\gamma\sigma_{01}$ (solid lines) is displayed in figure 15 for $0 \leqslant d \leqslant 350$. The damping coefficient d reaches the critical value d_c at the point marked A in the figure. The analytical solution is not plotted around this point since σ_{01} is undefined. Away from this singular point, the analytical solutions are in good quantitative agreement with the FISI 1 numerical modes. Their behaviour matches the one described above: the FISI 1 eigenvalues are complex conjugate for $d < d_c$ and purely real for $d > d_c$, d_c being equal to 302.2 in the numerical case. The asymptotic analysis thus gives two

solutions corresponding to the two FISI 1 modes and a good estimate of the different behaviours depending on the wall parameters; the collision/splitting of the FISI 1 mode on the real axis is produced in the asymptotic sense by a singularity when $d = d_c$.

When the higher order terms in the expansion are considered, the situation is more complex since the exchanges described in § 3.6 correspond to additional singularities in the asymptotic analysis. The solutions σ_{02} and σ_{20} are, respectively,

$$\sigma_{02} = \frac{1}{\sigma_{00} Re^2 (m+1)\left(\sigma_{00}^2 - \omega_0^2\right)} \left(4 - \frac{4}{3}\sigma_{00} Re - \frac{8}{15}\sigma_{00}^2 Re^2 + \frac{1}{6}\sigma_{00}^4 Re^2 - \frac{1}{4} E \sigma_{00}^2 - \frac{4}{\sqrt{\sigma_{00} Re}} \frac{\sinh(\sqrt{\sigma_{00} Re})}{\cosh(\sqrt{\sigma_{00} Re})} \right),$$

and

$$\sigma_{20} = \frac{\sigma_{00}^2}{(m+1)\left(\sigma_{00}^2 - \omega_0^2\right)} \left(\frac{\sigma_{00}}{3} - \frac{\sqrt{\sigma_{00}}}{\sqrt{Re}} \frac{\cosh\left(\sqrt{\sigma_{00} Re}\right)}{\sinh\left(\sqrt{\sigma_{00} Re}\right)} \right).$$

Each solution depends on σ_{00} and hence takes two different values. Both σ_{02} and σ_{20} present a singularity for $\sigma_{00} = \pm\, \omega_0$ ($d = d_c$), like σ_{01}. Furthermore, they present specific singularities when $\sinh(\sqrt{\sigma_{00} Re}) = 0$ for σ_{20} and $\cosh(\sqrt{\sigma_{00} Re}) = 0$ for σ_{02}, associated to specific behaviours in the spectrum, described below.

Let us first consider the case $\sinh(\sqrt{\sigma_{00} Re}) = 0$. This equation is verified when $\sqrt{\sigma_{00} Re} = \mathrm{i}\, k\, \pi$ with $k \in \mathbb{Z}$ which is not possible when $d < d_c$. When $d > d_c$, we have from (4.1)

$$\epsilon \sqrt{\frac{d^2}{d_c^2} - 1} = -\frac{k^2 \pi^2}{\omega_0 Re} + \frac{d}{d_c}, \tag{4.2}$$

providing the following conditions on d:

$$d \geqslant \frac{d_c}{\omega_0 Re} k^2 \pi^2 \quad \text{when } \epsilon = 1,$$
$$d \leqslant \frac{d_c}{\omega_0 Re} k^2 \pi^2 \quad \text{when } \epsilon = -1.$$

When the above conditions are verified, the solution of (4.2) is

$$d = \frac{d_c}{2\,\omega_0\, Re\, k^2\, \pi^2} \left(k^4 \pi^4 + \omega_0^2 Re^2 \right) \quad \text{with } k \in \mathbb{N}^*.$$

This means that, for $d > d_c$ (when the FISI 1 modes are real eigenvalues), for each value of $k \in \mathbb{N}^*$ one of the σ_{20} solution is undefined. For the parameters chosen, the eigenvalue corresponding to $\epsilon = 1$ verifies (4.2) for $k \leqslant 2$ with $d = 321.1$ and 840.2. The eigenvalue corresponding to $\epsilon = -1$ presents an infinity of singularities for $k \geqslant 3$.

Similarly, the equation $\cosh(\sqrt{\sigma_{00} Re}) = 0$ imposes $\sqrt{\sigma_{00} Re} = (2k+1)\,\mathrm{i}\,\pi$ with $k \in \mathbb{Z}$. A solution exists only for $d > d_c$

$$d = \frac{d_c}{2\,\omega_0\, Re\, (2k+1)^2\, \pi^2} \left((2k+1)^4 \pi^4 + 4\omega_0^2 Re^2 \right) \quad \text{with } k \in \mathbb{N}, \tag{4.3}$$

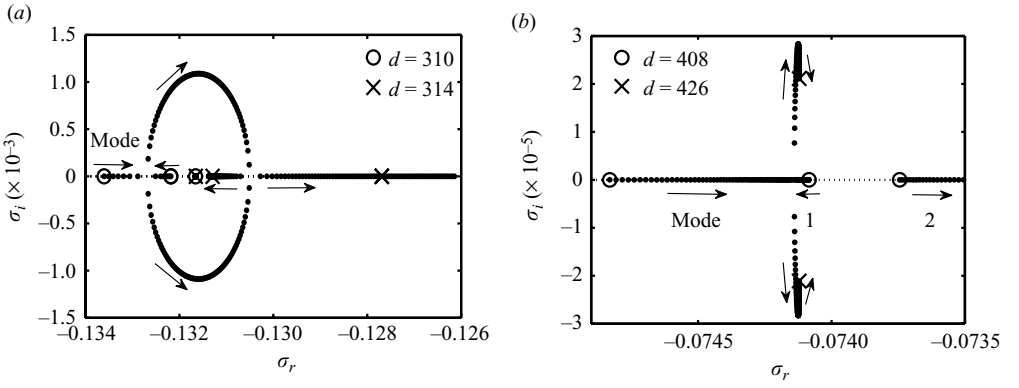

FIGURE 16. Zoom around point (*a*) *B* and (*b*) *C* from figure 15. Evolution of the numerical eigenvalue spectrum with d; (a) $310 \leqslant d \leqslant 315$ and (b) $405 \leqslant d \leqslant 426$. The mode followed with the asymptotic analysis before the intersection is labelled 'mode'. In figure (*b*), the eigenvalue labelled 2 is not visible for $d = 426$. Arrows denote increasing values of d.

and the compatibility conditions read

$$d \geqslant \frac{d_c}{4\omega_0 Re}(2k+1)^2\pi^2 \quad \text{when } \epsilon = 1,$$

$$d \leqslant \frac{d_c}{4\omega_0 Re}(2k+1)^2\pi^2 \quad \text{when } \epsilon = -1.$$

Also in this case, when (4.3) is verified, one of the σ_{02} solutions is undefined. This σ_{02} solution corresponds to $\epsilon = 1$ for $k \leqslant 2$ with $d = 426.9$ and 3249.7 and to $\epsilon = -1$ for $k \geqslant 3$.

For the parameters chosen here, once the FISI 1 modes have reached the real axis for $d \approx d_c$, the mode corresponding to $\epsilon = 1$ has a growth rate increasing with d while the mode corresponding to $\epsilon = -1$ has opposite behaviour. For $\epsilon = 1$, the mode followed by the asymptotic analysis will become very close to four centrifugal modes with the increase of d. These four centrifugal modes are visible for $d = 0$ in figure 15. Intersections between modes occur for values of the damping coefficient corresponding to singularities of σ_{02} and σ_{20}: $d \approx 311$, 417, 766 and 3200 in the numerical case. For $\epsilon = -1$, the same agreement is observed for all the intersections examined. Depending on the wall parameters, the quantitative agreement between the values of d corresponding to intersections and those obtained from (4.2) and (4.3) is more or less accurate: the closer to the rigid case, the better the quantitative agreement. Nevertheless, in every case considered, the number of intersections matches the number of singularities.

Four kinds of intersections have been observed. The first two involve the exchanges described in § 3.6; one is illustrated in figure 16(*a*) displaying a close-up of the numerical spectrum around the point marked *B* in figure 15. The growth rate of the FISI 1 mode increases with d until the eigenvalue reaches on the real axis a centrifugal mode whose growth rate decreases with d. The exchange occurs for $d = 310.2$ when both modes leave the real axis. For $d > 312.7$, the two modes reach again the real axis and their growth rates evolve in an opposite way with d, the asymptotic analysis always follows the mode which is more amplified. The second configuration is illustrated in figure 16(*b*) with a close-up of the numerical spectrum around the

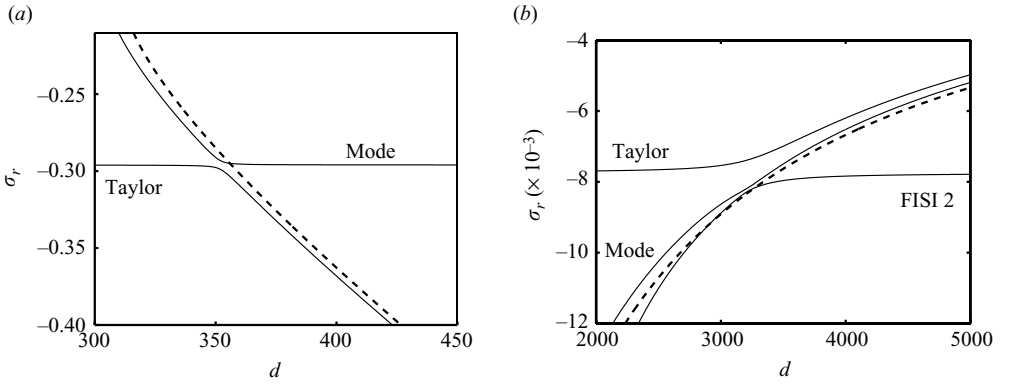

FIGURE 17. Eigenvalues growth rates versus d around point (a) D ($300 \leqslant d \leqslant 450$) and ($b$) E ($2000 \leqslant d \leqslant 50\,000$) from figure 15. σ_{00} is plotted in dotted line. The mode followed with the asymptotic analysis before the intersection is labelled 'mode' and other significant modes are labelled 'Taylor' (centrifugal mode) and 'FISI2'.

point marked C in figure 15. In that case, a second centrifugal mode (labelled 2 in figure 16b) is involved on top of that (labelled 1 in figure 16b) subject to the exchange. While the FISI 1 mode and the first centrifugal mode leave the axis for $d = 416.8$, the growth rate of the second centrifugal mode increases significantly so that it becomes the mode followed by the asymptotic analysis. Hence, for these two configurations, the modes followed before and after the exchange can be different.

The last two configurations are more easily handled if the growth rate of the involved (real) eigenvalues is plotted versus d. Figure 17(a) illustrates the behaviour of the spectrum around point D from figure 15. In this case, the mode followed by the asymptotic analysis and the centrifugal modes exchange their behaviour without meeting on the real axis, so that after the intersection, which occurs around $d \approx 352$, the analysis follows the Taylor mode (there is a singularity for $\epsilon = -1$ at $d = 356.5$). If one parameter other than d is slightly modified, the configuration undergoes the same kind of modal exchanges as described in the above paragraph. Finally, figure 17(b) displays the situation around the point marked E in figure 15. The two FISI 2 modes have reached the real axis for $d \approx 1724$; around $d \approx 3000$ (there is a singularity for $d = 3249$ when $\epsilon = 1$), the growth rates of the mode followed by the asymptotic analysis, one FISI 2 mode and one Taylor mode, display a break in slope.

To sum up, we have chosen to analyse the behaviour of solutions of the axisymmetric stability problem in the limit of small axial wavenumbers, in the form of integer powers of γ and β. With this expansion, two eigenvalues are found which means that other forms of developments should be considered to find the other eigenmodes. The two solutions obtained show different behaviour depending on the relative values of the wall parameters, and a critical value d_c of the damping coefficient has been highlighted. For $d < d_c$, the analytical eigenmodes show a very good quantitative agreement with the solutions obtained numerically for the FISI 1 modes. The change from complex conjugate eigenvalues to real ones of the FISI 1 modes for $d \approx d_c$ corresponds to a singularity in the analytical solutions. For $d > d_c$, the situation is rather complex. The terms of the expansion at high orders display additional singularities with modal exchanges. This short analysis then provides a way to systematically describe exchanges as function of the parameters.

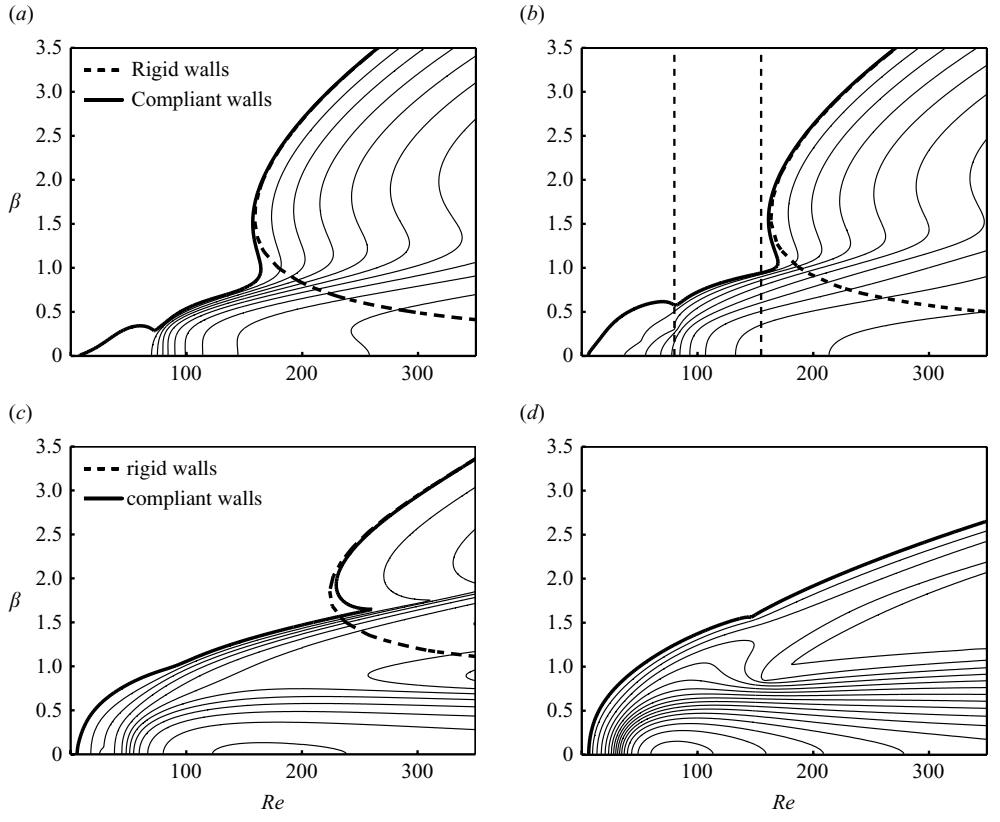

FIGURE 18. Neutral curves (thick lines) and curves of constant positive growth rates for different azimuthal wavenumbers in the compliant case (solid lines) and neutral curves for the rigid case (dashed lines) with (*a*) $n=1$, (*b*) $n=6$, (*c*) $n=20$ and (*d*) $n=40$. The spacing between two adjacent lines is $\Delta\sigma_r=0.004$. The wall parameters are $B=400$, $K=B/16$ and $d=0$. Vertical lines are drawn for $Re=80$ and $Re=155$ in (*b*).

5. Non-axisymmetric perturbations ($n\neq 0$)

5.1. *Influence of the azimuthal wavenumber*

When the walls are rigid, the critical Reynolds number increases linearly with n, meaning that the most unstable perturbation is axisymmetric. For the compliant case, the situation is more complex as seen in figure 18 where the isocontours of the zero and positive growth rate σ_r are plotted for different values of n ($n=1$, 6, 20 and 40). The neutral curve corresponds to $\sigma_r=0$ and is also plotted in dotted line for the rigid-wall case. For each azimuthal wavenumber, a break in slope in the neutral curve, for a given critical β_c value, separates the range of axial wavenumbers in two zones ($\beta_c\simeq 0.3$ when $n=1$, 0.6 when $n=6$ and 1.65 when $n=20$, β_c not shown in the figure for $n=40$).

In the axial wavenumber range above β_c, a comparison between neutral curves in the compliant- and rigid-wall cases indicates that the main instability is of centrifugal type (for $n=40$, the centrifugal mode appears for $Re>350$). Besides, as in the axisymmetric case (see figure 6), compliance has increased the range of unstable wavenumbers.

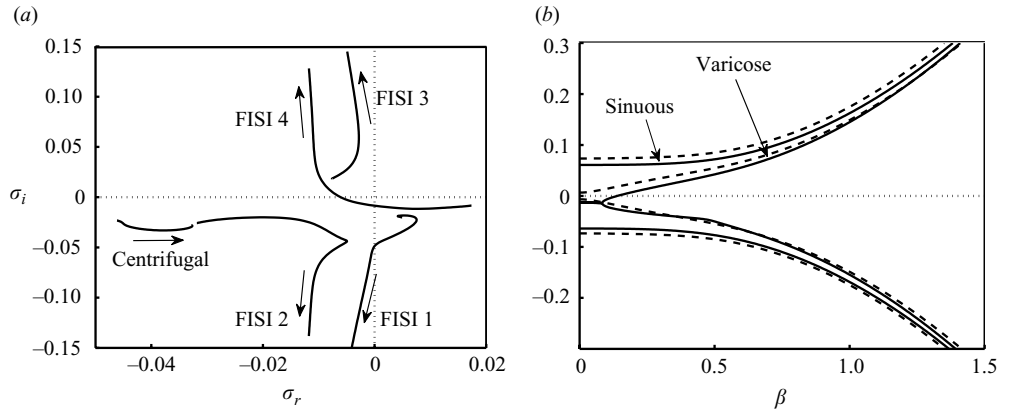

FIGURE 19. (*a*) Evolution of the main non-axisymmetric eigenvalues with β ($0 \leqslant \beta \leqslant 1$) for $n = 6$ and $Re = 80$. The wall parameters are $B = 400$, $K = B/16$ and $d = 0$. Arrows denote increasing β. (*b*) Frequency of the sinuous-like and varicose-like hydroelastic modes (solid lines) compared to the results obtained using the added mass model (dashed lines) for $n = 6$, $Re = 250$, $B = 4000$, $K = B/4$ and $d = 0$.

For axial wavenumbers smaller than β_c, the breaks in slope in the neutral curves denote the presence of a new (not centrifugal) large-wavelength unstable mode. The different figures show that the instability of this particular mode is initiated by two-dimensional perturbations with $\beta = 0$.

The presence of this second unstable mode is confirmed in figure 19(*a*) by examination of the evolution of the main eigenvalues with increasing β for $n = 6$ and $Re = 80$. As in the axisymmetric case, in addition to the centrifugal mode, four non-axisymmetric hydroelastic modes are generated by wall flexibility. For large values of β, two modes propagate with positive phase velocity ($\sigma_i < 0$) and the two remaining ones with negative phase velocity. These four modes are easily identifiable by continuation since σ_i increases (or decreases) significantly when β increases. We denote the least stable hydroelastic mode for large β's with a positive (negative) phase velocity by FISI 1 (FISI 3). The second hydroelastic mode with a positive (negative) phase velocity is called FISI 2 (FISI 4). As for the case $\alpha = 0$, the agreement between the frequency of the FISI modes and that obtained using the added mass model is satisfactory (cf. figure 19*b*), especially for large values of β for which the hydroelastic modes are coupled in pairs.

According to the spectrum in figure 19(*a*), the breaks in slope with β in the curves of constant positive growth rate are effectively related to the presence of two different unstable modes. These two unstable modes are the FISI 4 mode for $0 \leqslant \beta \leqslant 0.35$ and the FISI 1 mode for $0 \leqslant \beta \leqslant 0.58$. Accordingly, the curves of constant positive growth rate in figure 18(*b*) correspond to the predominant FISI 4 mode for $\beta < 0.31$, while they correspond to the predominant FISI 1 mode for $\beta > 0.31$.

The influence of the flexural rigidity B and of the spring stiffness K can be ascertained by inspection of figure 20 where neutral curves are displayed for two different azimuthal wavenumbers, $n = 6$ and $n = 21$. When B is fixed (cf. figures 20*a* and 20*b*), the influence of K is restricted to small axial wavenumbers and the critical Reynolds number decreases with K. When K is fixed (cf. figures 20*c* and 20*d*), the influence of B is small for large enough or small enough wavenumbers. The case $n = 21$ shows an opposite influence of B on hydroelastic and centrifugal modes. The

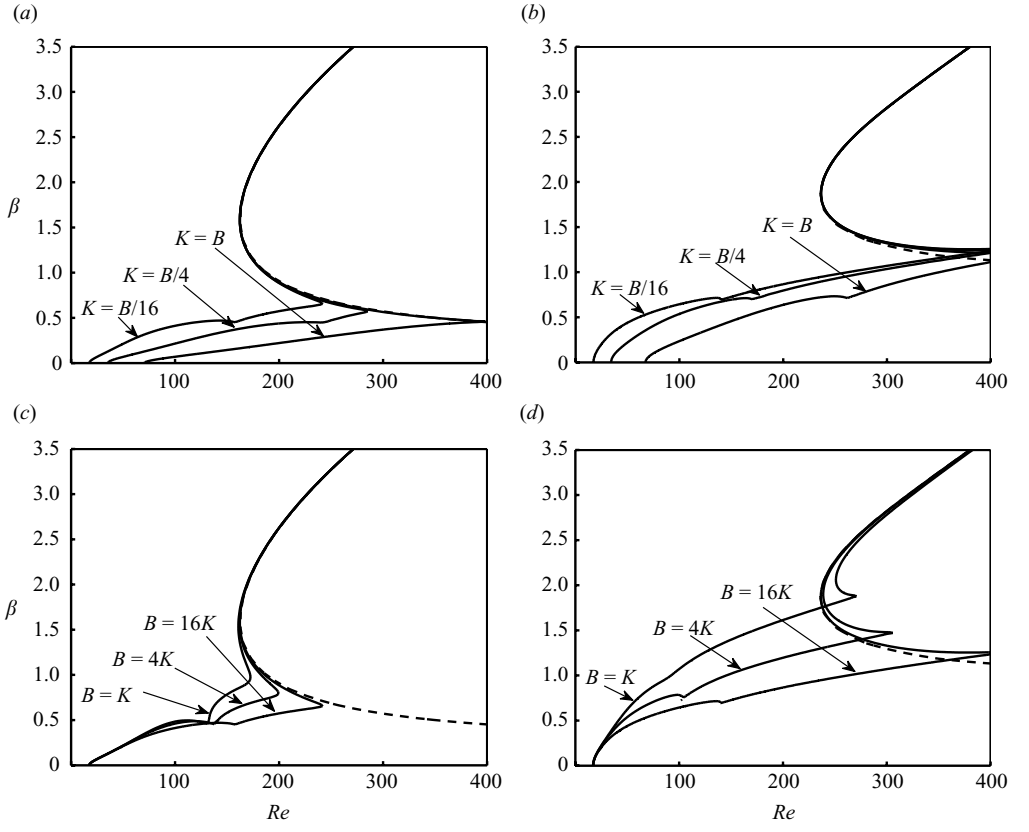

FIGURE 20. Neutral curves showing the influence of the spring stiffness K on non-axisymmetric instabilities for *a*) $B = 4000$; $n = 6$ and (*b*) $B = 4000$; $n = 21$ and the influence of the flexural rigidity B for *c*) $K = 250$; $n = 6$ and (*d*) $K = 250$; $n = 21$. In all cases $d = 0$. The dashed curve is the neutral curve in the rigid-wall case.

range of wavenumbers for which the centrifugal instability dominates (for β's above the breaks in slope) increases with B. On the contrary, the range over which the hydroelastic instability dominates (for β's below the breaks in slope) decreases with B. Moreover, the stabilizing influence of wall compliance on the large-wavenumber centrifugal instability increases with n, as can be inferred by comparison of the neutral curves in figures 20(*c*) and 20(*d*) with the rigid-wall case.

The influence of damping in the wall can be assessed from examination of figure 21. Neutral curves are displayed for different wall damping parameters and different n values, $n = 6$, 13 and 20, in figures 21(*a*), 21(*b*) and 21(*c*). Like for the parameters B and K, also d has little effect when β is large. Besides, once $d \neq 0$, the neutral curves for very low β's are all superposed to one another. In the middle β range, the situation is more complex because no general monotonic trend can be found. Attention should focus on the neutral curve for $d = 10$ near the points marked A and B in the figures (especially in figures 21*b* and 21*c*). Near point A, damping has a destabilizing influence while near point B it is stabilizing.

Analysis of the eigenvalue spectra confirm that the influence of d on non-axisymmetric eigenvalues is non-monotonic. This can be further assessed from figure 21(*d*) where the evolution of the main eigenvalues is plotted against d ($0 \leqslant d \leqslant 10\,000$) for

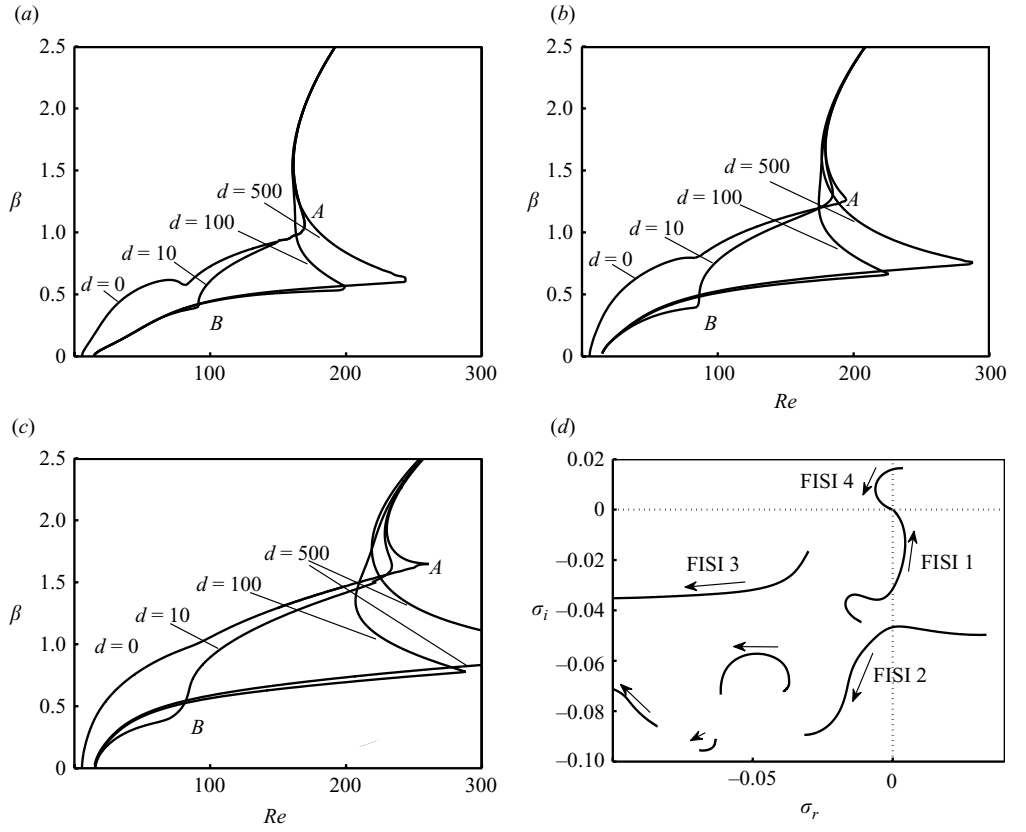

FIGURE 21. (*a*)–(*c*) Neutral curves showing the influence of wall damping for different non-zero azimuthal wavenumber with (*a*) $n=6$, (*b*) $n=13$ and (*c*) $n=20$. (*d*) Evolution of the main eigenvalues with d ($0 \leqslant d \leqslant 10\,000$) for $n=20$, $\beta=0.5$ and $Re=150$; arrows denote increasing d. The other wall parameters are $B=400$ and $K=B/16$.

$n=20$, $\beta=0.5$ and $Re=150$. The four hydroelastic modes are identified as explained above, all the other modes in the spectrum are of centrifugal origin. When d increases, both the FISI 1 and FISI 4 modes tend to collapse on the origin. Three different modes can be unstable depending on the value of d: the FISI 4 mode for $d < 10$, the FISI 2 mode for $d < 24$ and the FISI 1 mode for $d > 26$. But, while the FISI 2 growth rate decreases monotonically with d, the behaviour of the FISI 1 and FISI 4 modes is less simple: FISI 4 amplification is maximal for $d=0$ while FISI 1 growth rate is maximal for $d=78$. Analysis of spectra for other parameters shows the same complex behaviour, with different d extrema.

5.2. *Exchanges between non-axisymmetric modes*

A complete study of the case $n=6$ from figure 18(*b*) shows that, as in the axisymmetric case, it is difficult to dissociate the different modes with small axial wavenumbers due to exchanges between the eigenvalues. As already stated, figure 18(*b*) suggests that, for $Re \gtrsim 80$, a centrifugal-like mode predominates for all values of β. The spectrum shows that the unstable mode for $Re \gtrsim 80$ can belong to different branches depending on the value of the Reynolds number.

This can be understood in figure 22 where the evolution of the eigenvalue spectrum with β is presented for $n=6$ and for two very close values of the Reynolds number,

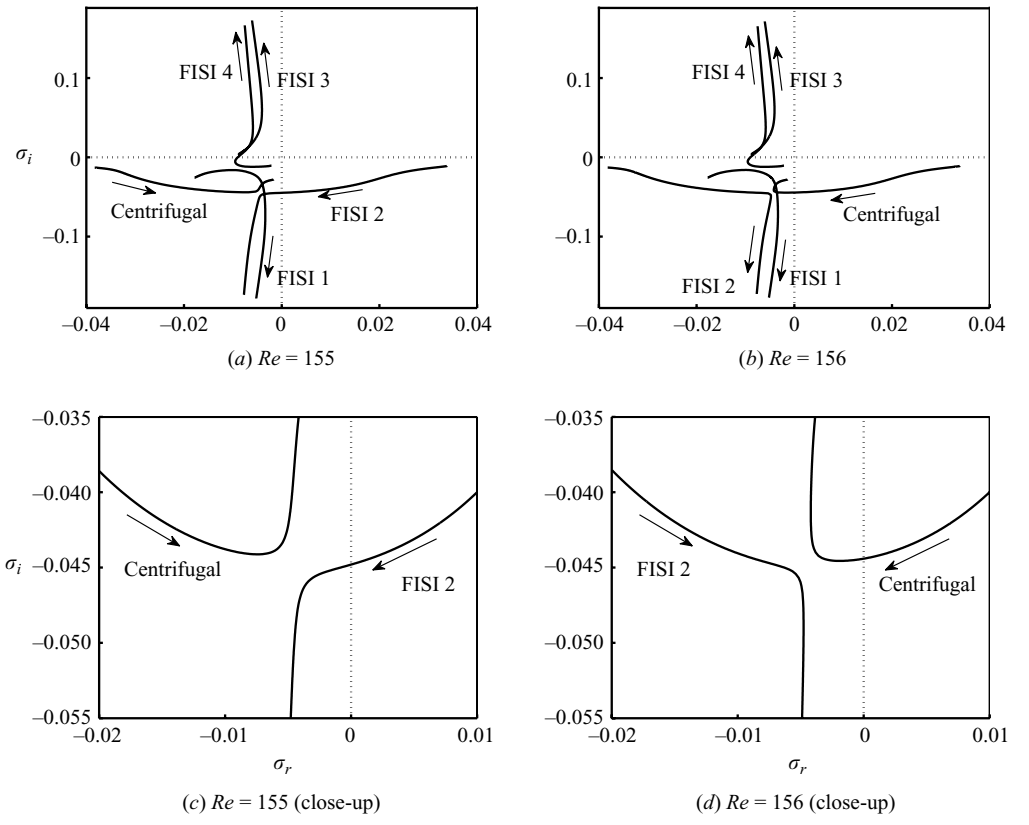

FIGURE 22. Exchange between one centrifugal and one FISI 2 non-axisymmetric modes. Evolution of the eigenvalue spectrum with β ($0 \leqslant \beta \leqslant 1.5$) for $n = 6$ and for (a) and (c) $Re = 155$ and (b) and (d) $Re = 156$. The wall parameters are $B = 400$, $K = B/16$ and $d = 0$. Arrows denote increasing β.

$Re = 155$ and 156. As already stated, the four hydroelastic modes are easily identified for large values of β because of their frequency. For the parameters considered, only one mode is unstable for $\beta \lesssim 0.94$. By continuously following the modes by drawing branches for decreasing β, it appears that this unstable mode belongs to a centrifugal branch for $Re = 155$ while it belongs to a FISI 2 branch for $Re = 156$. This is due to an exchange between the FISI 2 and the centrifugal stable modes for $\beta \simeq 0.95$ as can be seen in the close-up in figures 22(c) and 22(d). As the exchange involves stable modes, it is not visible in the curves of constant positive growth rate which remain continuous in figure 18(b).

Isocontours of azimuthal vorticity ω and velocity u for the four hydroelastic modes and the centrifugal mode with $n = 6$ are displayed in figure 23 when $Re = 155$ and $\beta = 0.5$. The same quantities are also presented in the rigid-wall case for the least stable mode. First, by comparing with the rigid-wall case, it is not easy to recognize the centrifugal mode when the walls are compliant. All the modes (except the FISI 1 mode) present characteristics similar to the centrifugal mode in the rigid case. Besides, the two modes submitted to an exchange for an axial wavenumber β close to that considered have similar structures. It is therefore impossible to distinguish the origin of each mode only by looking at their shapes, and only a continuous approach of the spectrum allows proper identification.

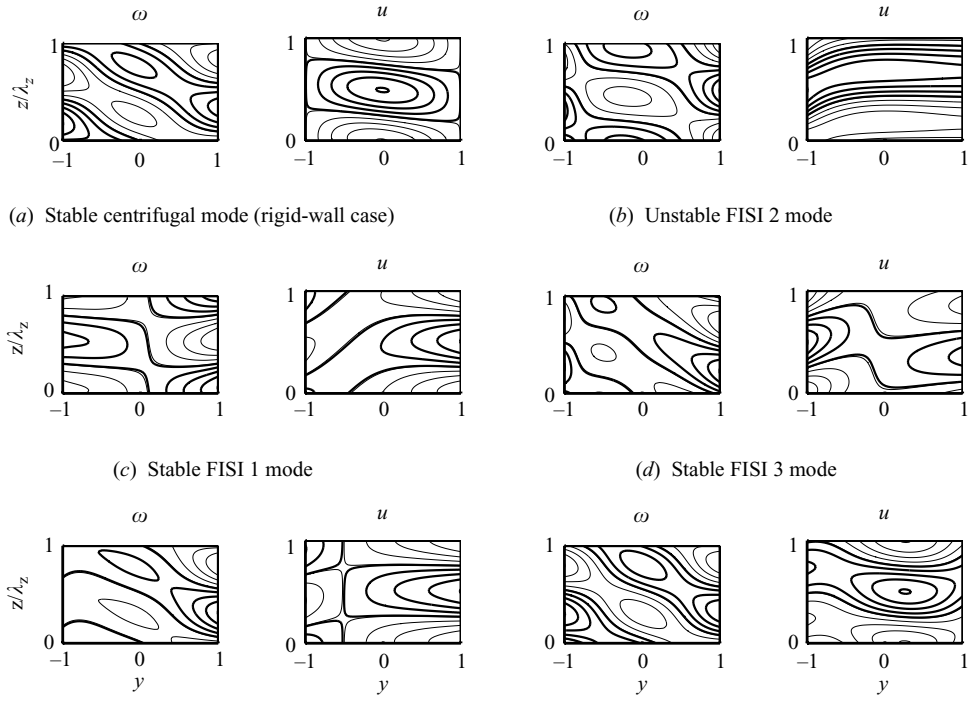

FIGURE 23. Isocontours of azimuthal vorticity ω and velocity u in the (y,z) plane for the $n=6$ modes with $Re=155$ and $\beta=0.5$. (a) Least stable centrifugal mode in the rigid-wall case; (b) to (f) main modes in the compliant-wall case (cf. figure 22a).

5.3. *Critical value n_c*

The neutral curves plotted in figure 18 in the $(Re,\ \beta)$ plane for different values of n have already shown that the most unstable perturbation is two-dimensional (with $\beta=0$) for each value of n. Thus, the axially homogeneous two-dimensional perturbations will now be considered separately. In figure 24 the neutral curves for the perturbations with $\beta=0$ are displayed in the $(Re,\ n)$ plane for different wall parameters. Note that the curves are plotted with continuous lines but are only defined for integer values of n. The neutral curves have quite complex shapes because different unstable modes predominate depending on the Re and n values. In figure 24(b), with B fixed at 4000, there exists a range of parameters for $n\simeq 150$ for which all the perturbations are stable, illustrated by the 'stable pockets' in the figure.

For each set of wall parameters there exists a critical non-zero n_c value for which the critical Reynolds number Re_c is minimal. The critical (Re_c, n_c) couple is marked with a black dot for each curve in figure 24. Critical values have been calculated for different wall parameters in the range $400\leqslant B\leqslant 40\,000$ with K in the range $B/16\leqslant K\leqslant 8\,B$ (cf. figure 25). From these values, a trend emerges: n_c depends on the ratio K/B and varies slowly with B. For instance, it is around $n_c=55$ for $K/B=1/2$ and $n_c=122$ for $K/B=4$ as can be seen in figure 25, meaning that, for the chosen value of γ, the azimuthal wavelength is equal to 13.13 units of length in the first case and 5.92 in the second.

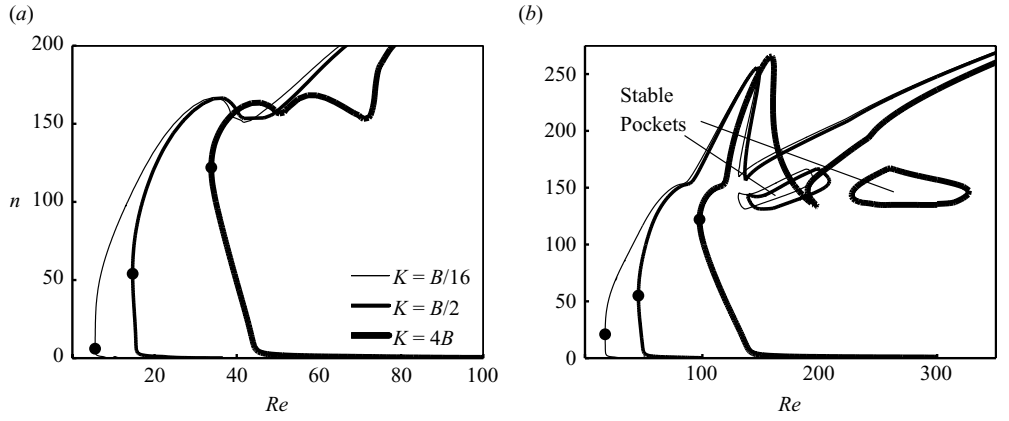

FIGURE 24. Neutral curves in the (Re, n) plane for axially homogeneous perturbations ($\beta = 0$) showing the existence of a critical most unstable n_c value for different spring stiffness with (*a*) $B = 400$ and (*b*) $B = 4000$ (and $d = 0$ in both cases). The black points mark the critical (Re_c, n_c) values for each curve. The critical n_c is (*a*) $n = 6$ for $K = B/16$, $n = 54$ for $K = B/2$, $n = 122$ for $K = 4B$, and (*b*) $n = 21$ for $K = B/16$, $n = 55$ for $K = B/2$, $n = 122$ for $K = 4B$.

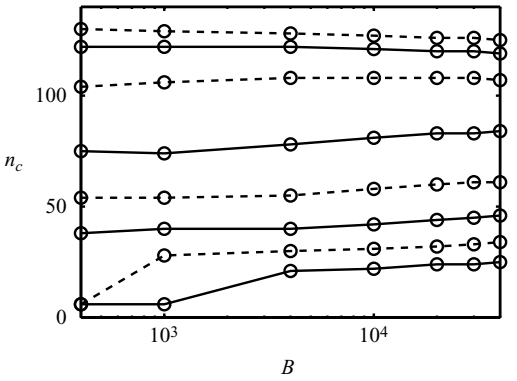

FIGURE 25. Critical value of n versus flexural rigidity B ($400 \leqslant B \leqslant 40\,000$) for different K/B ratios in the absence of wall damping. The calculated points are denoted by circles. The K/B ratio varies from 1/16 (lower curve) to 8 (higher curve) with a factor 2.

6. Concluding remarks

The linear analysis of the different modes of instability occurring in a Taylor–Couette system equipped with compliant walls has been carried out for the case of only the inner cylinder rotating. The compliant walls have been modelled as thin elastic shells supported by rigid frames through arrays of springs and dampers. Some of the results obtained are comparable to those found for the curved-channel flow (Guaus & Bottaro 2007), which also undergoes a centrifugal instability mechanism. The parametric study has not brought out compliant parameters capable of delaying the onset of the instability. Similar conclusions have been obtained by Kempf & McHugh (1996, 1998) and Koga and Nagata (cited by Carpenter & Pedley 2003) when only the outer cylinder is compliant. As for the curved-channel case, wall flexibility promotes the existence of four hydroelastic modes, whose phase velocities

can be estimated reasonably well by the simple added mass model developed by Hoepffner *et al.* (submitted). The main effect of compliance is to destabilize both hydrodynamic and hydroelastic modes of large wavelength, and the more so the softer the walls. An important conclusion is that, in opposition to the rigid-wall case, the most unstable modes are not the axisymmetric ones. Instability is initiated by a hydroelastic mode for a critical non-zero azimuthal wavenumber which depends on the compliant wall parameters, and in particular on the spring stiffness K. This mode has a two-dimensional structure, being homogeneous in the axial direction.

The study of the spectra turned out to be quite complex as it is difficult to distinguish the different unstable modes with large axial wavelengths, which are of interest. For small axial wavelengths, hydroelastic modes have very large phase velocities and hydrodynamic modes have eigenvalues in the spectrum very close to those in the rigid-wall case. Then, all modes are unmistakably identifiable. On the contrary, for large axial wavelengths, hydroelastic modes have eigenvalues close to the hydrodynamic ones. Due to exchanges between modes with identical eigenvalues, the same mode can be identified as hydrodynamic or hydroelastic depending on the Reynolds number considered. Similar exchanges have been observed by Levinski *et al.* (2001) for the case of the compliant wall-jet flow. The asymptotic analysis conducted for axisymmetric modes in the limit of small axial wavenumbers has highlighted interesting relations between the specific behaviours in the computed spectra and mathematical singularities of the analytical eigenmodes.

One particularity of the Taylor–Couette configuration (compared to the curved-channel flow case) is the behaviour of axisymmetric modes. The destabilization of large-wavelength centrifugal modes by compliant walls is essentially linked to energy exchanges with the mean flow. Whereas in the curved-channel case, the instability of streamwise-homogeneous hydroelastic disturbances is due to pairs of conjugate eigenvalues, possibly yielding a standing wave, here the instability of axisymmetric wall disturbances is initiated by a mode with zero phase velocity, provoking a static deformation of the walls.

Even in the limited frame of the linear stability analysis, this study has revealed the unexpected richness of behaviour of the Taylor–Couette system in the presence of flexible bounding walls, and it is the hope of the authors that the results herein will inspire and motivate future experimental and numerical investigations.

The first author acknowledges the support of a FLUBIO Marie Curie grant (MEST-CT-2005-020228) at the University of Genova, where this work was initiated.

Appendix

The metrics m_i and the operator L are

$$m_1 = \left(1 - \frac{\gamma}{2}y + \frac{\gamma^2}{4}y^2\right), \quad m_2 = \frac{\gamma}{2}\left(1 - \frac{\gamma}{2}y\right),$$

$$m_3 = \gamma(1 - \gamma y), \quad m_4 = \gamma y\left(1 - \frac{3}{4}\gamma y\right),$$

$$L = \left(\frac{\partial^2}{\partial x^2} + \frac{\partial^2}{\partial y^2} + \frac{\partial^2}{\partial z^2}\right) + m_2\frac{\partial}{\partial y} - m_4\frac{\partial^2}{\partial x^2}.$$

The generalized eigenvalue system is

$$0 = \mathrm{i}\alpha m_1 \hat{u} + D\hat{v} + \mathrm{i}\beta\hat{w} + m_2\hat{v},$$

$$\sigma\hat{u} = -\mathrm{i}\alpha m_1 U\hat{u} - U'\hat{v} - m_2 U\hat{v} - \mathrm{i}\alpha m_1\hat{p} + \frac{1}{Re}\left[\left(\hat{L} - \frac{\gamma^2}{4}\right)\hat{u} + \mathrm{i}\alpha m_3\hat{v}\right],$$

$$\sigma\hat{v} = -\mathrm{i}\alpha m_1 U\hat{v} + m_2 U\hat{u} - D\hat{p} + \frac{1}{Re}\left[\left(\hat{L} - \frac{\gamma^2}{4}\right)\hat{v} - \mathrm{i}\alpha m_3\hat{u}\right],$$

$$\sigma\hat{w} = -\mathrm{i}\alpha m_1 U\hat{w} - \mathrm{i}\beta\hat{p} + \frac{1}{Re}\hat{L}\hat{w},$$

with

$$D = \mathrm{d}/\mathrm{d}y, \quad U' = DU, \quad k^2 = \alpha^2 + \beta^2, \quad \hat{L} = D^2 - k^2 + m_2 D + \alpha^2 m_4.$$

REFERENCES

Argentina, M. & Mahadevan, L. 2005 Fluid-flow-induced flutter of a flag. *Proceedings of the National Academy of Sciences of the United States of America*, **102**, 1829–1834.

Benjamin, T. B. 1960 Effects of a flexible boundary on hydrodynamic stability. *J. Fluid Mech.* **9**, 513–532.

Benjamin, T. B. 1963 The threefold classification of unstable disturbances in flexible surfaces bounding inviscid flows. *J. Fluid Mech.* **16**, 436–450.

Buckingham, A. C., Hall, M. S. & Chun, R. C. 1985 Numerical simulations of compliant material response to turbulent flow. *AIAA J.* **23**, 1046–1052.

Bushnell, D. M., Hefner, J. N. & Ash, R. L. 1977 Effect of compliant wall motion on turbulent boundary layers. *Phys. Fluids* A **20**, S31.

Carpenter, P. W. 1990 Status of transition delay using compliant walls. In *Viscous Drag Reduction in Boundary Layers* (ed. D. M. Bushnell and J. N. Hefner), pp. 79–113. AIAA.

Carpenter, P. W. 1993 Optimization of multiple-panel compliant walls for delay of laminar–turbulent transition. *AIAA J.* **31**, 1187–1188.

Carpenter, P. W., Davies, C. & Lucey, A. D. 2000 Hydrodynamics and compliant walls: does the dolphin have a secret? *Curr. Sci.* **79**, 758–765.

Carpenter, P. W. & Garrad, A. D. 1985 The hydrodynamic stability of flow over Kramer-type compliant surfaces. Part 1. Tollmien–Schlichting instabilities. *J. Fluid Mech.* **155**, 465–510.

Carpenter, P. W. & Garrad, A. D. 1986 The hydrodynamic stability of flow over Kramer-type compliant surfaces. Part 2. Flow-induced surface instabilities. *J. Fluid Mech.* **170**, 199–232.

Carpenter, P. W. & Morris, P. J. 1990 The effect of anisotropic wall compliance on boundary-layer stability and transition. *J. Fluid Mech.* **218**, 171–223.

Carpenter, P. W. & Pedley, T. J. 2003 Editors of *IUTAM Symposium on Flow Past Highly Compliant Boundaries and in Collapsible Tubes*. Kluwer Academic Publishers.

Carpenter, P. W. & Thomas, P. J. 2007 Flow over compliant rotating disks. *J. Engng Math.* **57**, 303–315.

Chandrasekhar, S. 1981 *Hydrodynamic and Hydromagnetic Stability*. Dover.

Colley, A. J., Carpenter, P. W., Thomas, P. J., Ali, R. & Zoueshtiagh, F. 2006 Experimental verification of Type-II-eigenmode destabilization in the boundary layer over a compliant rotating disk. *Phys. Fluids* **18**, 054107.

Colley, A., Thomas, P. J., Carpenter, P. W. & Cooper, A. J. 1999 An experimental study of boundary-layer transition over a rotating disk. *Phys. Fluids* **11**, 3340–3352.

Cooper, A. J. & Carpenter, P. W. 1997*a* The effect of wall compliance on inflexion point instability in boundary layers. *Phys. Fluids* **9**, 468–470.

Cooper, A. J. & Carpenter, P. W. 1997*b* The stability of rotating-disk boundary-layer flow over a compliant wall. Part 2. Absolute instability. *J. Fluid Mech.* **350**, 261–270.

Couette, M. 1890 Etudes sur le frottement des liquides. *Ann. Chim. Phys.* **21**, 433–510.

Davies, C. & Carpenter, P. W. 1997*a* Instabilities in a plane channel flow between compliant walls. *J. Fluid Mech.* **352**, 205–243.

Davies, C. & Carpenter, P. W. 1997*b* Numerical simulation of the evolution of Tollmien–Schlichting waves over finite compliant panels. *J. Fluid Mech.* **335**, 361–392.

Denier, J. P. & Hall, P. 1991 The effect of wall compliance on the Görtler vortex instability. *Phys. Fluids* A **3**, 2000–2002.

Domaradzki, J. A. & Metcalfe, R. W. 1987 Stabilization of laminar boundary layers by compliant membranes. *Phys. Fluids* **30**, 695–705.

Drazin, P. G. & Reid, W. H. 1981 *Hydrodynamic Stability*. Cambridge University Press.

Duncan, J. H., Waxman, A. M. & Tulin, M. P. 1985 The dynamics of waves at the interface between a viscoelastic coating and a fluid flow. *J. Fluid Mech.* **158**, 177–197.

Ehrenstein, U. & Rossi, M. 1996 Nonlinear Tollmien–Schlichting waves for a Blasius flow over compliant coatings. *Phys. Fluids* **32**, 256–267.

Gad-el-Hak, M. 1986 The response of elastic and viscoelastic surfaces to a turbulent boundary layer. *J. Appl. Mech.* **53**, 206–212.

Gad-el-Hak, M. 2002 Compliant coatings for drag reduction. *Prog. Aerosp. Sci.* **38**, 77–99.

Gad-el-Hak, M., Blackwelder, R. F. & Riley, J. J. 1984 On the interaction of compliant coatings with boundary-layer flows. *J. Fluid Mech.* **140**, 257–280.

Gaster, M. 1987 Is the dolphin a red herring? *In IUTAM Symposium on Turbulence Management and Relaminarisation* (ed. H. W. Liepmann and R. Narasimha), pp. 285. Springer.

Guaus, A. 2008 Analyse linéaire des instabilités dans les écoulements incompressibles à parois courbes compliantes. PhD thesis, Université Toulouse III – Paul Sabatier.

Guaus, A. & Bottaro, A. 2007 Instabilities of the flow in a curved channel with compliant walls. *Proc. R. Soc. London* A **463**, 2201–2222.

Hoepffner, J., Bottaro, A. & Favier, J. Submitted. Mechanisms of non-modal energy amplification in channel flow between compliant walls. *J. Fluid Mech.*

Joslin, R. D. & Morris, P. J. 1992 Effect of compliant walls on secondary instabilities in boundary-layer transition. *AIAA J.* **30**, 332–339.

Joslin, R. D., Morris, P. J. & Carpenter, P. W. 1991 Role of three-dimensional instabilities in compliant wall boundary-layer transition. *AIAA J.* **29**, 1603–1610.

Kempf, M. & McHugh, J. 1996 Stability of Taylor–Couette flow with an elastic layer on the outer cylinder. *APS Division of Fluids Dynamics Meeting*. Oral communication.

Kempf, M. & McHugh, J. 1998 Fluid-structure interaction in Taylor–Couette flow. *APS Division of Fluids Dynamics Meeting*. Oral communication.

Kramer, M. O. 1957 Boundary-layer stabilization by distributed damping. *J. Aero. Sci.* **24**, 459–460.

Kramer, M. O. 1960*a* Boundary-layer stabilization by distributed damping. *J. Am. Soc. Nav. Engrs* **72**, 25–33.

Kramer, M. O. 1960*b* The dolphin's secret. *New Scientist* **7**, 1118–1120.

Kramer, M. O. 1965 Hydrodynamics of the dolphin. *Adv. Hydrosci.* **2**, 111–130.

Landahl, M. T. 1962 On the stability of a laminar incompressible boundary layer over a flexible surface. *J. Fluid Mech.* **13**, 609–632.

Levinski, V., Levy, D.-E. & Cohen, J. 2001 Effects of wall compliance on the hydrodynamic stability and transition delay of a wall-jet flow. *Fluid Dyn. Res.* **29**, 115–134.

Lucey, A. D., Cafolla, G. J. & Carpenter, P. W. 1997*a* Numerical simulation of a boundary-layer flow interacting with a passive compliant boundary. *Lecture Notes Phys.* **490**, 406–411.

Lucey, A. D., Cafolla, G. J. & Carpenter, P. W. 1998 The effect of a boundary layer on the hydroelastic stability of a flexible wall. In *Proceedings of the Third International Conference on Engineering Aero-Hydroelasticity*, Prague. pp. 268–273.

Lucey, A. D., Cafolla, G. J., Carpenter, P. W. & Yang, M. 1997*b* The nonlinear hydroelastic behaviour of flexible walls. *J. Fluid. Struct.* **11**, 717–744.

Lucey, A. D. & Carpenter, P. W. 1992 A numerical simulation of the interaction of a compliant wall and an inviscid flow. *J. Fluid Mech.* **234**, 121–146.

Mallock, A. 1888 Determination of the viscosity of water. *Proc. R. Soc. Lond.* A **45**, 126–132.

Mallock, A. 1896 Experiments on fluid viscosity. *Phil. Trans. R. Soc. Lond.* A **187**, 41–56.

Prigent, A. & Dauchot, O. 2000 "Barber pole turbulence" in large aspect ratio Taylor-Couette flow. arXiv:cond-mat/0009241 v1 15 Sept. 2000.

Riley, J. J., Gad-el-Hak, M. & Metcalfe, R. W. 1988 Compliant coatings. *Annu. Rev. Fluid Mech.* **20**, 393–420.

Sen, P. K. & Arora, D. S. 1988 On the stability of laminar boundary-layer flow over a flat plate with a compliant surface. *J. Fluid Mech.* **197**, 201–240.

Taylor, G. I. 1923 Stability of a viscous liquid contained between two rotationg cylinders. *Phil. Trans. R. Soc. Lond.* A **223**, 289–343.

Timoshenko, S. & Woinowsky-Krieger, S. 1959 *Theory of Plates and Shells*. McGraw–Hill.

Wiplier, O. & Ehrenstein, U. 2000 Numerical simulation of linear and nonlinear disturbance evolution in a boundary layer with compliant walls. *J. Fluid. Struct.* **14**, 157–182.

Yeo, K. S. 1988 The stability of boundary-layer over single- and multi-layer viscoelastic walls. *J. Fluid Mech.* **196**, 359–408.

Yeo, K. S., Khoo, B. C. & Chong, W. K. 1994 The linear stability of boundary-layer over compliant walls: effects of boundary-layer growth. *J. Fluid Mech.* **280**, 199–225.

Yeo, K. S., Khoo, B. C. & Zhao, H. Z. 1996 The absolute instability of boundary-layer flow over viscoelastic walls. *Theor. Comp. Fluid Dyn.* **8**, 237–252.

Yurchenko, N. F. & Babenko, V. V. 1987 Stability criterion of three-dimensional perturbations on concave elastic surfaces. *J. Engr. Phys. Thermophys.* **52**, 568–573.